

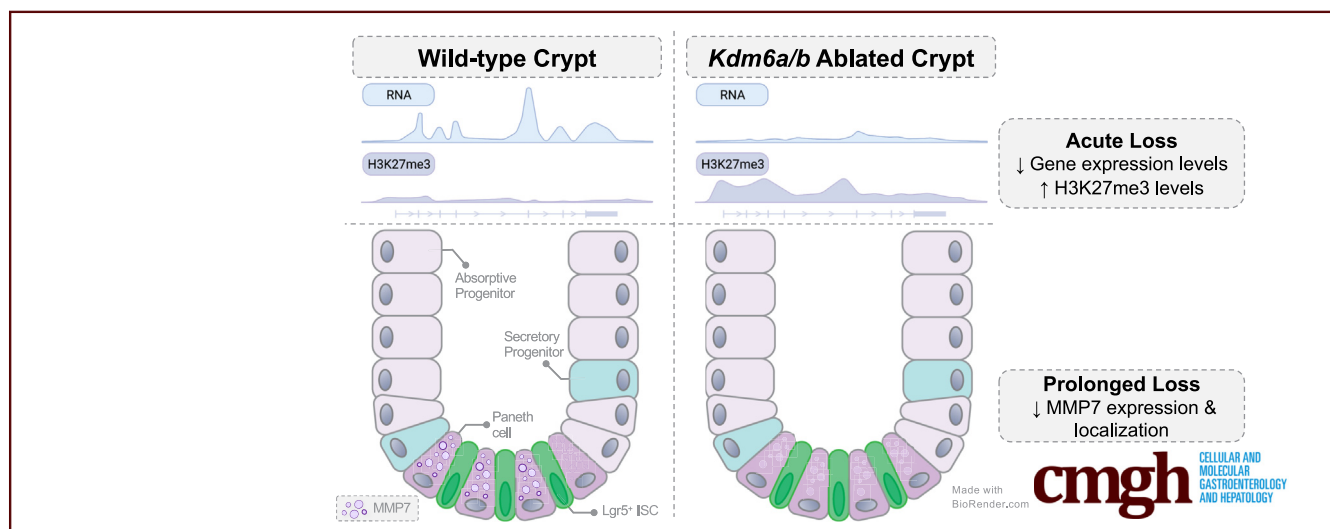
ORIGINAL RESEARCH

H3K27me3 Demethylases Maintain the Transcriptional and Epigenomic Landscape of the Intestinal Epithelium



Hannah M. Kolev,^{1,2} Avital Swisa,^{1,2} Elisabetta Manduchi,^{1,2} Yemin Lan,^{3,4} Rachel R. Stine,^{2,3} Giuseppe Testa,^{5,6} and Klaus H. Kaestner^{1,2}

¹Department of Genetics, Perelman School of Medicine, University of Pennsylvania, Philadelphia, Pennsylvania; ²Institute for Diabetes, Obesity, and Metabolism, Perelman School of Medicine, University of Pennsylvania, Philadelphia, Pennsylvania; ³Department of Cell and Developmental Biology, Perelman School of Medicine, University of Pennsylvania, Philadelphia, Pennsylvania; ⁴Penn Epigenetics Institute, Perelman School of Medicine, University of Pennsylvania, Philadelphia, Pennsylvania; ⁵Department of Experimental Oncology, European Institute of Oncology, Istituto di Ricovero e Cura a Carattere Scientifico, Milan, Italy; and ⁶Department of Oncology and Hemato-Oncology, University of Milan, Milan, Italy



SUMMARY

The histone H3 lysine 27 demethylases lysine (K)-specific demethylase 6A and lysine (K)-specific demethylase 6B were studied in the intestinal epithelium of adult mice. Although dispensable for intestinal homeostasis and regeneration, lysine (K)-specific demethylase 6A/B regulate specific intestinal gene expression programs and histone H3 lysine 27 patterns.

BACKGROUND & AIMS: Although trimethylation of histone H3 lysine 27 (H3K27me3) by polycomb repressive complex 2 is required for intestinal function, the role of the antagonistic process—H3K27me3 demethylation—in the intestine remains unknown. The aim of this study was to determine the contribution of H3K27me3 demethylases to intestinal homeostasis.

METHODS: An inducible mouse model was used to simultaneously ablate the 2 known H3K27me3 demethylases, lysine (K)-specific demethylase 6A (*Kdm6a*) and lysine (K)-specific demethylase 6B (*Kdm6b*), from the intestinal epithelium. Mice were analyzed at acute and prolonged time points after *Kdm6a/b* ablation. Cellular proliferation and differentiation were

measured using immunohistochemistry, while RNA sequencing and chromatin immunoprecipitation followed by sequencing for H3K27me3 were used to identify gene expression and chromatin changes after *Kdm6a/b* loss. Intestinal epithelial renewal was evaluated using a radiation-induced injury model, while Paneth cell homeostasis was measured via immunohistochemistry, immunoblot, and transmission electron microscopy.

RESULTS: We did not detect any effect of *Kdm6a/b* ablation on intestinal cell proliferation or differentiation toward the secretory cell lineages. Acute and prolonged *Kdm6a/b* loss perturbed expression of gene signatures belonging to multiple cell lineages (adjusted *P* value < .05), and a set of 72 genes was identified as being down-regulated with an associated increase in H3K27me3 levels after *Kdm6a/b* ablation (false discovery rate, <0.05). After prolonged *Kdm6a/b* loss, dysregulation of the Paneth cell gene signature was associated with perturbed matrix metalloproteinase 7 localization (*P* < .0001) and expression.

CONCLUSIONS: Although KDM6A/B does not regulate intestinal cell differentiation, both enzymes are required to support the full transcriptomic and epigenomic landscape of the intestinal epithelium and the expression of key Paneth cell genes.

(*Cell Mol Gastroenterol Hepatol* 2023;15:821–839; <https://doi.org/10.1016/j.jcmgh.2022.12.001>)

Keywords: ChIP-Seq; KDM6A; KDM6B; Lgr5⁺ ISCs; Paneth Cells; PRC2.

The small intestinal epithelium is maintained by a population of rapidly cycling intestinal stem cells (ISCs). Marked by *Lgr5* expression, these ISCs reside at the base of epithelial invaginations termed *crypts of Lieberkühn* and divide symmetrically to produce absorptive and secretory progenitor cells.^{1–4} Absorptive progenitor cells proliferate in a process called transit amplification as they migrate out of the crypt base and up the crypt wall. Upon exiting the crypt and entering finger-like projections termed villi, absorptive progenitors differentiate to produce mature absorptive enterocytes. Secretory progenitors do not undergo transit amplification but differentiate progressively to give rise to the secretory cell types of the epithelium, which include goblet cells, enteroendocrine cells, tuft cells, and Paneth cells.⁵

The carefully orchestrated process of cellular differentiation is driven largely by dramatic shifts in the transcriptional program as differentiating ISCs cease to express their stem cell-specific gene program and initiate cell type-specific gene activity.⁶ Well-defined signaling pathways and lineage-specific transcription factors help orchestrate these shifts in gene activity. However, recently, the epigenetic mechanisms regulating transcriptional reprogramming during ISC differentiation have become the topics of intense investigation. Epigenetic modifiers, such as the *Polycomb* group proteins, control cellular differentiation by determining chromatin compaction, which in turn prevents or enables lineage-defining transcription factors to bind DNA and determine cell identity.⁷


The polycomb repressive complex 2 (PRC2) consists of multiple proteins including the catalytically active enzymes enhancer of zeste homolog 1 and 2, as well as the structural proteins suppressor of zeste 12 and embryonic ectoderm development.⁸ PRC2 maintains cellular identity by catalyzing the monomethylation, dimethylation, and trimethylation of histone H3 lysine 27 (H3K27me1/2/3), resulting in the transcriptional repression of target genes.⁹ In intestinal crypts, PRC2 plays a dual role in promoting cell proliferation and preventing aberrant differentiation toward the secretory lineage.^{10–12} Loss of PRC2 activity in the intestinal epithelium depletes H3K27me3 and reactivates genes involved in cell-cycle arrest and secretory lineage specification.^{11,12} Accordingly, ablation of the required PRC2 component *embryonic ectoderm development* from the intestinal epithelium of adult mice results in decreased numbers of proliferating cells and increased numbers of goblet cells and enteroendocrine cells.^{11,12} Conversely, inappropriate stabilization of enhancer of zeste homolog 2 results in perturbed Paneth cell differentiation, homeostasis, and functioning.¹³ Chromatin immunoprecipitation followed by sequencing (ChIP-seq) specifically in ISCs identified suppressor of zeste 12 binding and an associated

accumulation of H3K27me3 at key secretory lineage-defining transcription factors,¹² suggesting that PRC2 functions in ISCs to prevent premature differentiation toward the secretory lineage. Together, results from these studies bring into question whether the subsequent differentiation of ISCs requires removal of the repressive epigenetic layer placed by PRC2. However, the function of active H3K27me3 demethylation in the intestinal epithelium remains unknown.

To address this critical knowledge gap, we investigated the function of the only identified H3K27me3 demethylases, lysine (K)-specific demethylase 6A (KDM6A) and lysine (K)-specific demethylase 6B (KDM6B), in the intestinal epithelium. KDM6A and KDM6B, also termed *ubiquitously transcribed tetratricopeptide repeat gene X chromosome* and *jumonji domain containing 3*, respectively, catalyze the demethylation of H3K27me3.^{14–17} *Kdm6a* resides on the X chromosome and escapes X inactivation.¹⁸ Ubiquitously transcribed tetratricopeptide repeat gene Y chromosome (UTY), the male paralog of *Kdm6a*, previously was considered catalytically inactive¹⁷; however, UTY retains modest demethylase activity and can partially compensate for KDM6A.^{19,20}

Given the ability to revert PRC2-mediated gene repression, KDM6A and KDM6B are critical for gene activation during differentiation in many developing and self-renewing tissues, including embryonic stem cells^{21,22} and the hematopoietic,²³ epidermal,²⁴ and muscle compartments.^{25,26} Indeed, *Kdm6a* deficiency in mice results in embryonic lethality owing to failed cardiac development, whereas *Kdm6b* null mice are perinatal lethal as a consequence of failed neuronal development.^{21,27} In adult tissues, KDM6A demethylates H3K27me3 at the *Myogenin* promoter after muscle injury to promote myoblast differentiation.²⁶ Similarly, KDM6B activates expression of key epidermal differentiation genes during calcium-induced differentiation of human keratinocytes.²⁴ Furthermore, simultaneous removal of both *Kdm6a* and *Kdm6b* from intrathymic CD4⁺ T-cell precursors blocks late stages of T-cell development, owing largely to a failure to remove H3K27me3 at genes involved in terminal differentiation.²⁸ Importantly, disruption of either *Kdm6a* or *Kdm6b* alone yields a less-pronounced

Abbreviations used in this paper: ChIP-seq, chromatin immunoprecipitation followed by sequencing; DKO, double-knockout; EdU, 5-thymyl-2'-deoxyuridine; FDR, false discovery rate; GSEA, gene set enrichment analysis; H3K27me3, histone H3 lysine 27 trimethylation; IGV, Integrative Genomics Viewer; ISC, intestinal stem cell; KDM6A, lysine (K)-specific demethylase 6A; KDM6B, lysine (K)-specific demethylase 6B; LiCl, –; MMP7, matrix metalloproteinase 7; mRNA, messenger RNA; PBS, phosphate-buffered saline; PRC2, polycomb repressive complex 2; RNA-seq, RNA sequencing; RT-qPCR, quantitative reverse-transcription polymerase chain reaction; SDS, sodium dodecyl sulfate.

 Most current article

© 2022 The Authors. Published by Elsevier Inc. on behalf of the AGA Institute. This is an open access article under the CC BY-NC-ND license (<http://creativecommons.org/licenses/by-nc-nd/4.0/>).

2352-345X

<https://doi.org/10.1016/j.jcmgh.2022.12.001>

phenotype, demonstrating the overlapping functions of KDM6A and KDM6B in differentiating CD4⁺ T cells.^{28,29}

Together, these studies show that KDM6A- and KDM6B-mediated H3K27me3 demethylation is an important epigenetic process regulating cellular differentiation during development and adult tissue homeostasis. However, whether KDM6A and KDM6B are required for cellular differentiation in the intestinal epithelium remains unknown. In the present study, we use an inducible, intestine-specific mouse model of simultaneous *Kdm6a* and *Kdm6b* deficiency to elucidate the function of H3K27me3 demethylases during adult intestinal homeostasis.

Results

To determine the function of H3K27me3 demethylases in the intestinal epithelium, we simultaneously ablated both *Kdm6a* and *Kdm6b* (*Kdm6a/b*) expression, thereby presumably removing any H3K27me3 demethylase activity. We generated *Kdm6a*^{f/f}; *Kdm6b*^{f/f}; *Villin-Cre*^{ERT2} double-knockout (DKO) mice, in which the *Villin* promoter drives expression of tamoxifen-inducible Cre recombinase specifically in the intestinal epithelium. Adult control (*Kdm6a*^{f/f}; *Kdm6b*^{f/f}) and DKO mice were treated for 3 consecutive days with tamoxifen to induce Cre activity, and intestinal tissue was analyzed 7 days (acute ablation model) or 5 months (prolonged ablation model) later (Figure 1A). To mitigate any H3K27me3 demethylase compensation by UTY,²⁰ female mice were used for all experiments. Efficient gene ablation was confirmed via immunohistochemistry for KDM6A protein (Figure 1B) and quantitative reverse-transcription polymerase chain reaction (RT-qPCR) for *Kdm6a* and *Kdm6b* messenger RNA (mRNA) (Figure 1C). Importantly, genetic ablation of both *Kdm6a* and *Kdm6b* mRNA persisted 5 months after induction of genetic ablation (Figure 1C), suggesting a lack of competitive pressure selecting for any crypt cells that might have escaped Cre-mediated recombination.

To identify the earliest consequences of *Kdm6a/b* loss, we used the acute ablation model and analyzed intestinal tissue 7 days after the final tamoxifen dose. First, we employed immunohistochemistry to determine whether KDM6A/B are required for cell proliferation and differentiation toward the secretory lineages in the jejunum. We stained for the proliferation marker protein Ki-67 (hereafter referred to as Ki-67), a protein expressed only in proliferating cells, as well as markers of mature secretory cell types including chromogranin A to mark enteroendocrine cells and lysozyme to mark Paneth cells. We also used Alcian blue staining to visualize the acidic mucin-positive goblet cells. Surprisingly, we observed no differences in cell proliferation (Figure 2A) or differentiation toward the goblet cell (Figure 2B), Paneth cell (Figure 2C), or enteroendocrine cell (Figure 2D) lineages when comparing control and DKO mice. Given the increasing evidence of significant regionalization along the gastrointestinal tract,³⁰ we also evaluated KDM6A/B function in a more distal region of the intestine. We analyzed the ileum of control and DKO mice after acute *Kdm6a/b* ablation and completed immunohistochemistry as

described earlier. Consistent with our findings from the jejunum, we did not detect any statistically significant difference in the number of proliferating cells (Figure 3A) or differentiation toward the secretory lineages (Figure 3B–D) in the ileum of DKO mice. Finally, prolonged ablation of *Kdm6a/b* yielded similar results because differentiation toward the goblet cell, Paneth cell, and enteroendocrine cell lineages remained unchanged 5 months after induction of gene ablation (data not shown). Together, these findings demonstrate that KDM6A/B are dispensable for cell proliferation and cell lineage allocation in the intestinal epithelium.

Next, we asked whether KDM6A/B are required to maintain the transcriptomic landscape of the intestinal epithelium. We collected intestinal epithelial cells from the crypts of control and DKO mice after acute and prolonged ablation and completed bulk RNA sequencing (RNA-seq). A total of 382 genes were differentially expressed at the acute time point ($n = 5\text{--}7$ per group; adjusted P value $\leq .05$; fold-change, ≥ 2). Consistent with the known function of *Kdm6a/b* in facilitating gene activation, the majority of the differentially expressed genes (262) were down-regulated in DKO mice (Figure 4A). At the prolonged time point, a total of 364 genes were expressed differentially ($n = 3\text{--}5$ per group; adjusted P value $\leq .05$; fold-change, ≥ 2), of which 225 were down-regulated in DKO mice (Figure 4B). A total of 176 genes were expressed differentially at both the acute and prolonged time points (Figure 4C). To understand the functional significance of these gene expression changes, we performed gene set enrichment analysis (GSEA)³¹ using published gene signatures of intestinal cell lineages.^{32–35} We found that at both the acute and prolonged time points, signatures of mature cell types, including Paneth cells, enteroendocrine cells, tuft cells, and distal enterocytes, were down-regulated in DKO mice (Figure 4D and E). In addition, both acute and prolonged *Kdm6a/b* ablation down-regulated the *Lgr5*⁺ ISC, secretory progenitor, and enterocyte progenitor signatures (Figure 4D–G), and the *Lgr5*⁺ ISC signature was the most dysregulated signature at the acute time point. A subset of differentially expressed genes identified at both the acute and prolonged time points were validated via RT-qPCR (Figure 4H and I). Together, these data suggest that although cellular differentiation remains intact in DKO mice (Figures 2 and 3), *Kdm6a/b* are required to maintain the expression of intestinal epithelial cell gene signatures (Figure 4), and in their absence the intestinal epithelium is susceptible to significant shifts in gene activity.

We next used ChIP-seq for H3K27me3 to identify genomic regions that are direct targets of KDM6A/B demethylase activity. To determine the earliest H3K27me3 changes associated with *Kdm6a/b* loss, we performed ChIP-seq 7 days after induction of gene ablation in DKO mice. A total of 378 genomic regions with differential H3K27me3 signals were identified, and 228 genes were associated with increased H3K27me3 levels in DKO mice ($n = 4$ per group) (Figure 5A). Thus, our ChIP-seq data did not show a global increase in H3K27me3 across the genome, but rather

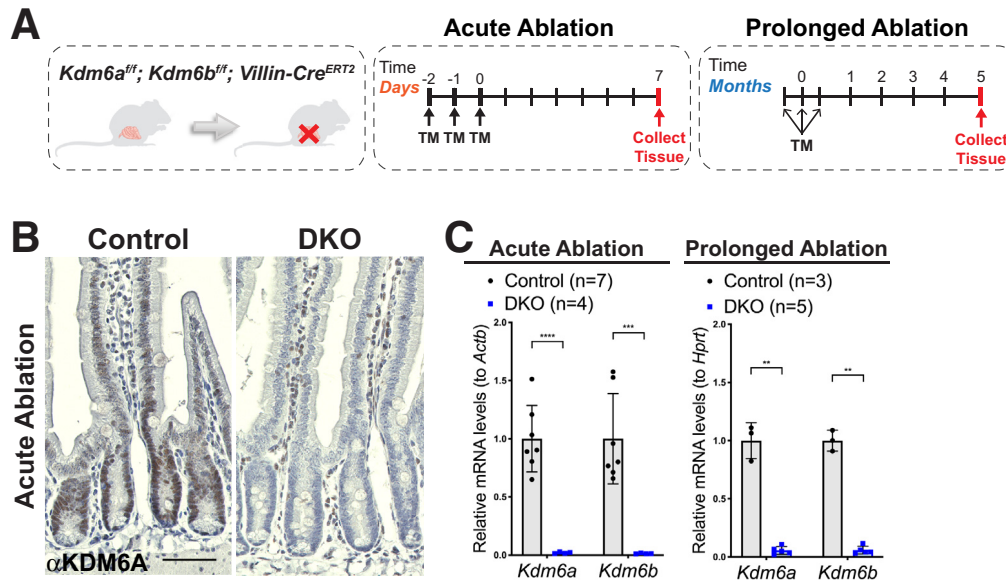


Figure 1. *Kdm6a* and *Kdm6b* gene expression is ablated from the intestinal epithelium of *Kdm6a^{fl/fl}; Kdm6b^{fl/fl}; Villin-Cre^{ERT2}* mice. (A) Tamoxifen (TM) injection scheme for control (*Kdm6a^{fl/fl}; Kdm6b^{fl/fl}*) and DKO (*Kdm6a^{fl/fl}; Kdm6b^{fl/fl}; Villin-Cre^{ERT2}*) mice. Mice were treated with tamoxifen once daily for 3 consecutive days and analyzed 7 days (middle panel, acute ablation model) or 5 months (right panel, prolonged ablation model) later. (B) Genetic ablation was confirmed 7 days after tamoxifen treatment via immunohistochemistry for KDM6A. (C) Genetic ablation was confirmed 7 days and 5 months after tamoxifen treatment via RT-qPCR for *Kdm6a* and *Kdm6b* mRNA. Statistical comparisons were made using the Student's *t* test with Welch's correction. *n* = 3–7 per group. ***P* < .01, ****P* < .001, and *****P* < .0001. Scale bar: 50 μ m.

localized changes in H3K27me3 levels at a subset of genes. To confirm this finding, we completed immunohistochemistry for H3K27me3 in control and DKO mice after acute *Kdm6a/b* ablation. Consistent with our ChIP-seq results, we did not observe a significant increase in H3K27me3 levels in DKO mice (Figure 5B), suggesting that in the absence of *Kdm6a/b*, increased H3K27me3 levels are restricted to a subset of loci rather than being increased universally across the genome.

We next compared those genes showing increased H3K27me3 levels with those that are down-regulated in DKO mice. To identify the maximum possible overlap, no fold-change cut-off value was used for the down-regulated genes when making this comparison. A total of 16,517 genes were covered in both the RNA-seq and ChIP-seq analyses. Of these, 1,258 genes were down-regulated, and 191 genes were associated with increased H3K27me3 levels in DKO mice, with a significant overlap of 72 genes (expected overlap = 15; *P* < 2.2e-16 with both the chi-square and Fisher exact tests) (Figure 5C). Consistent with the observed down-regulation of the *Lgr5⁺* ISC signature after *Kdm6a/b* ablation (Figure 4D and F), we identified 9 *Lgr5⁺* ISC signature genes with decreased mRNA and increased H3K27me3 levels in DKO mice (Figure 5C). Integrative Genomics Viewer (IGV) (Broad Institute)³⁶ tracks of *Slc14a1* and *Afap1l1*, 2 representative *Lgr5⁺* ISC signature genes,³⁵ show decreased mRNA expression and increased H3K27me3 levels in DKO mice (Figure 5D and E). Together, these data suggest that genetic ablation of *Kdm6a/b* results in modest changes in H3K27me3, which partially overlap with *Lgr5⁺* ISC signature genes.

Given the observed impairment of the *Lgr5⁺* ISC gene signature in DKO mice, we next asked whether *Kdm6a/b* are required for intestinal stem cell renewal during homeostasis and after intestinal damage. We began by using an EdU (5-ethynyl-2'-deoxyuridine) incorporation assay to identify changes in homeostatic intestinal crypt cell renewal in DKO mice. EdU, a thymidine analog, is incorporated into the DNA of cells during S phase of the cell cycle and therefore is a robust marker of DNA synthesis and cell replication.³⁷ Control and DKO mice were analyzed 7 days after tamoxifen treatment and were injected with EdU 2 hours prior to sacrifice. Analysis of the number of EdU⁺ cells per crypt in the jejunum of control and DKO mice showed no statistically significant difference (Figure 6A), suggesting that homeostatic epithelial cell renewal as measured by EdU incorporation does not require KDM6A/B activity.

In addition to homeostatic self-renewal, the intestinal epithelium also has the remarkable capacity to regenerate after damage. Given its high mitotic index, the intestinal epithelium is highly susceptible to ionizing radiation and other DNA damaging agents, which induce extensive apoptosis of proliferative *Lgr5⁺* ISCs and transit-amplifying cells.³⁸ After radiation-induced cell death, a regenerative response characterized by crypt enlargement and increased cell proliferation repopulates intestinal crypts and restores the crypt-villus architecture.³⁸ This robust regenerative response is mediated by multiple cell types, including dedifferentiating crypt progenitors as well as surviving *Lgr5⁺* cells.^{39–46} We took advantage of the high degree of regeneration induced by radiation damage to determine whether compromised expression of the *Lgr5⁺* ISC gene

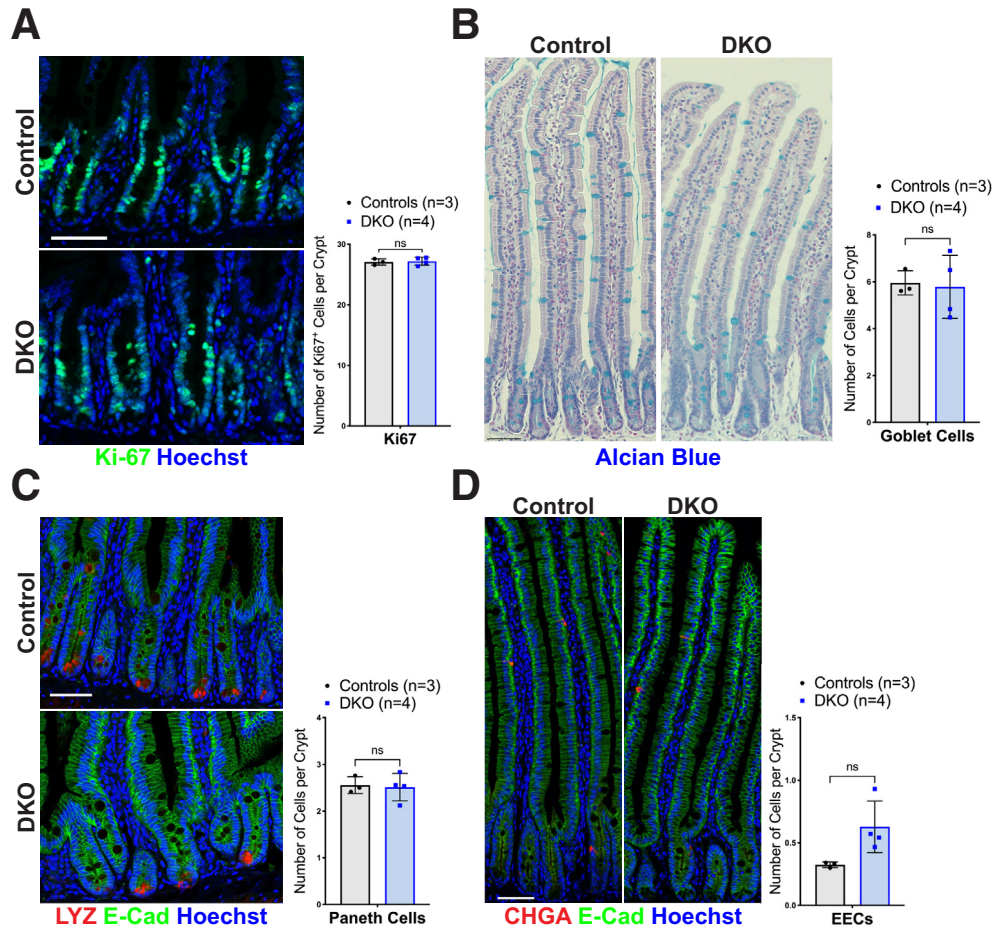


Figure 2. KDM6A and KDM6B are dispensable for intestinal epithelial cell proliferation and lineage allocation in the proximal jejunum. (A) Epithelial cell proliferation is maintained in DKO mice, as measured by immunohistochemistry for Ki-67. (B) Differentiation of intestinal epithelial cells toward the goblet cell lineage is maintained in DKO mice, as measured by Alcian blue staining. (C) Differentiation of intestinal epithelial cells toward the Paneth cell lineage is maintained in DKO mice, as measured by immunohistochemistry for lysozyme (LYZ). (D) Differentiation toward the enteroendocrine cell (EEC) lineage is maintained in DKO mice, as measured by immunohistochemistry for chromogranin A (CHGA). Statistical comparisons were made using the Student's *t* test with Welch's correction. Mice were analyzed after acute *Kdm6a/b* ablation (7 days). *n* = 3–4 per group. Scale bars: 50 μ m. E-cad, E-cadherin. Ki-67, proliferation marker protein Ki-67.

signature in DKO mice sensitizes the mice to radiation damage and perturbs intestinal epithelial cell renewal. Seven days after tamoxifen treatment, control and DKO mice were subjected to 14 Gy irradiation. Mice were killed 4 days after radiation treatment during the regenerative phase of recovery, and epithelial cell renewal was measured via EdU incorporation into regenerative crypt foci (Figure 6B and C). Under these experimental conditions, we did not detect any significant difference in the number of regenerative crypt foci per unit distance or the number of EdU⁺ cells per regenerative crypt foci when comparing control and DKO mice (Figure 6D). These findings show that intestinal epithelial cell renewal, both during homeostasis and after radiation-induced damage, does not require KDM6A/B activity. Taken together with our gene expression analyses, our results suggest that impaired expression of the *Lgr5*⁺ ISC gene signature is not sufficient to perturb the robust epithelial cell renewal process in DKO mice.

Finally, in addition to the observed function of KDM6A/B in regulating expression of the *Lgr5*⁺ ISC gene signature, we also identified a role for the enzymes in maintaining expression of mature cell type signatures (Figure 4D and E). In particular, the Paneth cell gene signature was down-regulated after both acute and prolonged *Kdm6a/b* ablation (Figure 7A and C) and was the most statistically significantly down-regulated gene signature after prolonged gene ablation. Analysis of individual Paneth cell marker genes identified down-regulation of multiple defensins and antimicrobial peptides in DKO mice (Figure 7B and D). Surprisingly, we did not identify increased H3K27me3 levels at Paneth cell marker genes, defensins, or other antimicrobial peptides.

Interestingly, acute and prolonged *Kdm6a/b* ablation resulted in significant down-regulation of the Paneth cell marker gene *Mmp7* (Figure 7E), which encodes an enzyme required for proteolytic activation of defensins and thus is

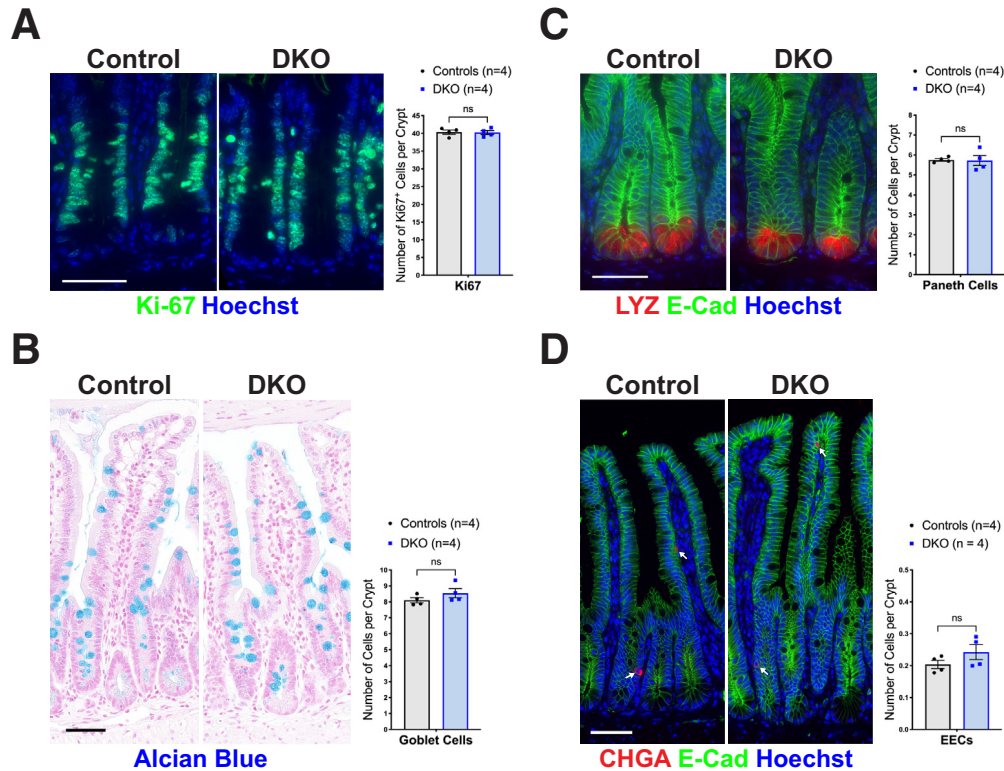


Figure 3. Cell proliferation and lineage allocation remains unchanged in the ileum after acute *Kdm6a/b* ablation. (A) Immunohistochemistry for Ki-67 identifies no statistically significant difference in cell proliferation in the ileum of DKO mice. (B) Differentiation of intestinal epithelial cells toward the goblet cell lineage remains intact in the ileum of DKO mice, as measured by Alcian blue staining. Differentiation of intestinal epithelial cells toward the Paneth cell and enteroendocrine cell (EEC) lineages remains intact in the ileum of DKO mice, as measured by immunohistochemistry for (C) lysozyme (LYZ) and (D) chromogranin A (CHGA, *arrows*), respectively. Statistical comparisons were made using the Student's *t* test with Welch's correction. Mice were analyzed after acute *Kdm6a/b* ablation (7 days). *n* = 4 per group. Scale bars: 50 μ m. E-cad, E-cadherin. Ki-67, proliferation marker protein Ki-67.

critical for Paneth cell microbicidal activity and host defense against infection.^{47,48} Seeking to better understand the effect of *Kdm6a/b* loss on *Mmp7* expression, we used immunohistochemistry to evaluate matrix metalloproteinase 7 (MMP7) localization patterns in Paneth cells of DKO mice. Given the extended half-life of Paneth cells (~60 days),⁴⁹ we analyzed DKO mice after prolonged *Kdm6a/b* ablation to observe the most significant effects of *Kdm6a/b* loss on MMP7 localization. In control mice, MMP7 showed a punctate staining pattern, consistent with its localization to Paneth cell secretory granules (Figure 7F). However, after prolonged *Kdm6a/b* ablation, MMP7 adopted a more diffuse staining pattern, with a reduced percentage of MMP7-expressing cells showing a punctate staining pattern (Figure 7F). To assess whether this diffuse staining pattern may reflect reduced MMP7 protein expression in DKO mice, we completed Western blot analysis for MMP7 after prolonged *Kdm6a/b* ablation. Although statistical significance was not reached, we identified a trend toward decreased MMP7 protein expression in DKO mice (Figure 7G). Interestingly, transmission electron microscopy analysis of Paneth cells in control and DKO mice did not identify a change in the number of electron-dense secretory granules per Paneth cell, the percentage area of the Paneth cell occupied

by secretory granules, or the average granule area (Figure 7H), suggesting that the diffuse MMP7 staining pattern is not a result of perturbed secretory granule formation in DKO mice. Together, these data indicate that *Kdm6a/b* are required for expression of the Paneth cell gene signature and that prolonged absence of *Kdm6a/b* expression results in disrupted MMP7 localization, with a slight reduction in MMP7 protein expression.

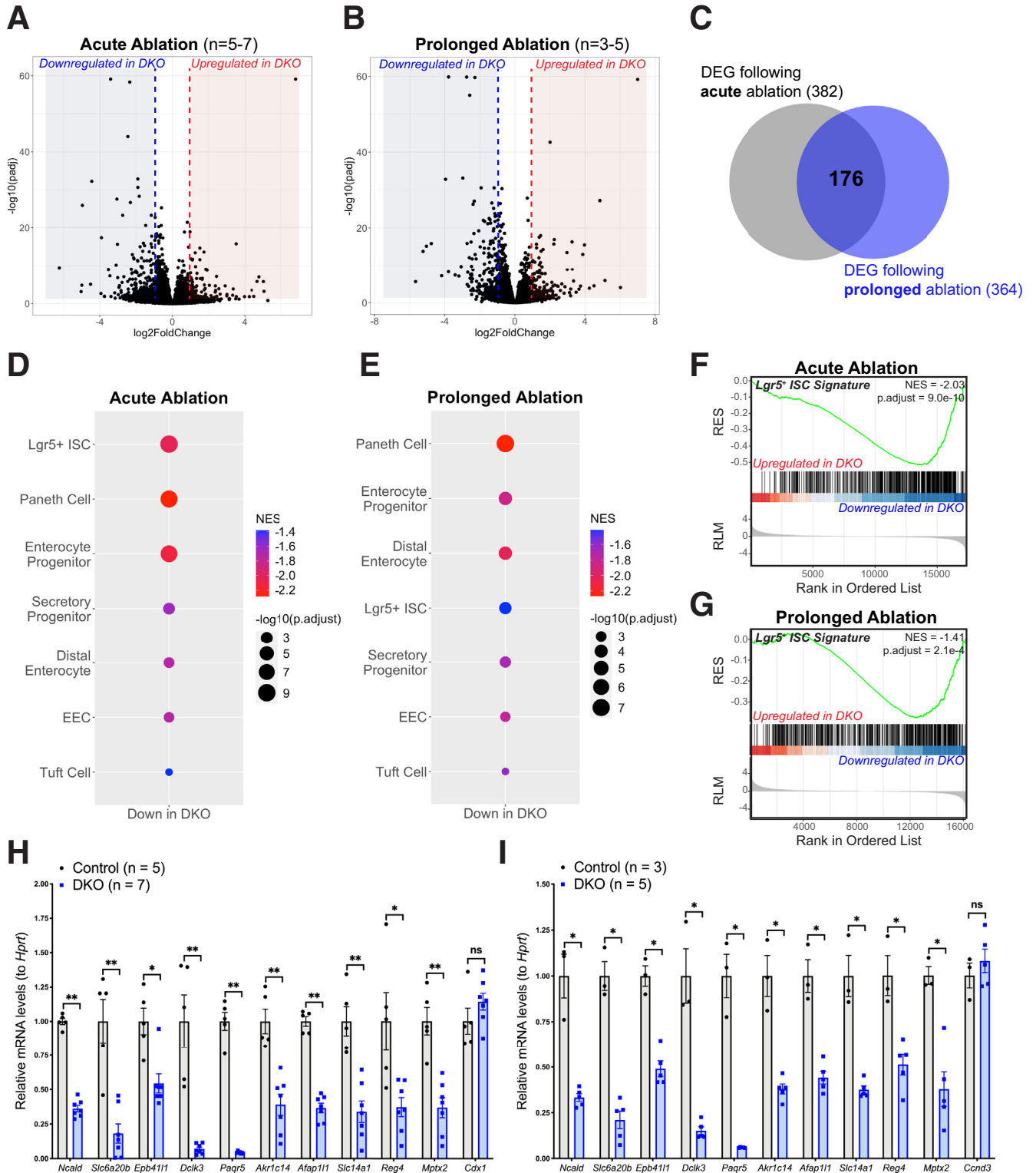
Together, our studies investigating KDM6A and KDM6B function suggest that these 2 enzymes support the transcriptomic and epigenomic landscape of the intestinal epithelium despite being dispensable for intestinal cell differentiation and self-renewal.

Discussion

Accurate execution of cell type-specific gene expression programs and cell lineage allocation are critical for maintaining intestinal homeostasis. Epigenetic processes such as PRC2-mediated gene silencing are critical determinants of cell type-specific gene activity, and, thus, cell fate determination. Although many studies have dissected the mechanism by which PRC2 regulates intestinal homeostasis by H3K27me3 deposition, the role of the antagonistic process—H3K27me3 demethylation—in the intestine

remains unexplored. In the present study, we investigated the function of KDM6A and KDM6B, the only identified H3K27me3 demethylases, specifically in the mammalian intestine.

By removing both *Kdm6a* and *Kdm6b* in the intestinal epithelium of adult mice, we determined that intestinal homeostasis functions by and large independently of H3K27me3 demethylase activity. At the cellular level,



differentiation toward the secretory lineages remained intact in both the jejunum and ileum after *Kdm6a/b* inactivation. At the genomic level, we identified a modest role for KDM6A/B in maintaining accurate gene expression through H3K27me3 removal, as 72 genes were down-regulated with an associated increase in H3K27me3 after *Kdm6a/b* ablation. Although we identified a set of 9 *Lgr5*⁺ ISC signature genes that are regulated by *Kdm6a/b*, we found that homeostatic and injury-induced renewal of the intestinal epithelium does not require KDM6A/B activity. Our findings of limited KDM6A/B involvement in regulating cellular dynamics and the transcriptional and epigenomic environment of the intestinal epithelium are surprising given the critical function of PRC2 in the intestine. First, PRC2 maintains cell proliferation in intestinal crypts through transcriptional repression of *Cdkn2a*, which encodes the cell-cycle inhibitors p16^{INK4A} and p19^{ARF}.^{10–12,50} Second, by transcriptionally repressing secretory lineage-defining transcription factors, such as *Atoh1* and *Gfi1*, PRC2 prevents premature differentiation of *Lgr5*⁺ ISCs and transit-amplifying cells toward the secretory lineages.^{11,12} Finally, PRC2 maintains crypt cell plasticity during radiation-induced regeneration, and *Eed* inactivation before radiation injury results in failed crypt regeneration and subsequent mortality.¹² Our findings indicate that active H3K27me3 demethylation is not required to antagonize PRC2-mediated regulation of cell proliferation, differentiation, or regeneration, and, thus, the rapid cellular turnover of the intestinal epithelium occurs independently of H3K27me3 demethylases.

Our findings of modest KDM6A/B function in the intestine, together with our understanding of PRC2 activity in the intestinal epithelium, suggest that an alternative mechanism might be operating to revert the repressive effects of PRC2 on gene expression and cellular dynamics. We propose that one such mechanism involves the passive dilution of H3K27me3-marked nucleosomes during cellular replication.⁵¹ During symmetric cell division, epigenetic patterns must be faithfully inherited by daughter cells to ensure epigenetic memory; however, the process of DNA replication is inherently disruptive and requires breakdown of the nucleosome.⁵² Thus, to preserve H3K27me3 patterns, daughter cells inherit parental H3K27me3-marked nucleosomes and incorporate naïve, unmodified nucleosomes that undergo *de novo* modification via PRC2 recruitment.^{53,54} If H3K27me3 is not actively added on these newly

incorporated nucleosomes, parental H3K27me3-marked nucleosomes are diluted out at each successive round of cellular division.^{55,56} Given that transit-amplifying cells divide up to 6 times in intestinal crypts before terminal differentiation,^{57,58} simply turning off PRC2 components or redirecting the PRC2 complex away from target loci in these progenitor cells would enable H3K27me3 removal via replicational dilution.

A recent study provided support for replicational dilution as the primary mode of H3K27me3 decay in intestinal epithelial cells.⁵¹ After PRC2 inactivation in the intestinal epithelium, the rapidly dividing transit-amplifying compartment lost H3K27me3 and reactivated PRC2 target genes more rapidly than the slower-dividing *Lgr5*⁺ ISC population. Furthermore, inactivation of PRC2 specifically within *Lgr5*⁺ ISCs resulted in uniform reduction of H3K27me3 levels across the genome, and computational modeling of dilution-mediated H3K27me3 decay showed that PRC2-deficient ISCs lose H3K27me3 at a rate matching what would be expected given the published ISC replication rate. Thus, in this context, auxiliary processes, such as active H3K27me3 demethylation, are not required for H3K27me3 loss across the genome. Importantly, the rate of target gene reactivation after PRC2 depletion is dependent not only on the number of cell divisions, but also on promoter poising, or rather, the abundance of the active methylation mark H3K4me3 at gene promoters.^{10,51} Thus, active demethylation by KDM6A/B may not be required to remove H3K27me3 in most cases; instead, genes that lose H3K27me3 may do so via replicational dilution and may be transcriptionally activated at a rate dependent on their level of promoter poising.

Given the evidence of replication dilution as a primary means of H3K27me3 removal, the question arises as to why *Kdm6a/b* are expressed throughout the intestinal epithelium. Our observations of increased H3K27me3 levels at a small fraction of genes after *Kdm6a/b* ablation suggest that these enzymes may function as a fail-safe mechanism to ensure appropriate levels of H3K27me3 in intestinal epithelial cells. Indeed, previous investigations of KDM6B occupancy at p53-bound promoters and enhancers suggest that rather than contributing to the direct activation of p53 target genes, KDM6B may function as a fail-safe to maintain low levels of H3K27me3 and enable post-translational modification of other histones, such as acetylation of

Figure 4. (See previous page). *Kdm6a/b* loss perturbs the transcriptomic landscape of the intestinal epithelium. RNA-seq analysis of intestinal epithelial cells collected from the crypts of control and DKO mice after (A) acute and (B) prolonged gene ablation identifies up-regulated and down-regulated transcripts. Blue shaded box represents all transcripts that are down-regulated with a fold-change of at least 0.5 and an adjusted *P* value < .05. Red shaded box represents all transcripts that are up-regulated with a fold-change of at least 2 and an adjusted *P* value < .05. Dashed lines represent a fold-change of 0.5 (blue) and 2 (red). *n* = 3–7 per group. (C) Venn diagram depicting the overlap of differentially expressed genes (DEGs) between the acute and prolonged time points. GSEA using intestinal cell type gene signatures identifies a suite of signatures that are enriched in genes down-regulated after (D) acute and (E) prolonged *Kdm6a/b* ablation. Gene sets are listed in descending order based on $-\log_{10}$ (adjusted *P* value). GSEA plots showing down-regulation of the *Lgr5*⁺ ISC gene signature after (F) acute and (G) prolonged *Kdm6a/b* ablation. RT-qPCR analysis confirms a subset of down-regulated genes after (H) acute and (I) prolonged *Kdm6a/b* ablation. (H) *Cdx1* and (I) *Ccnd3* were included as negative control genes. Statistical comparisons were made using the Mann–Whitney test with correction for multiple comparisons made by controlling the FDR. **q* < 0.05, ***q* < 0.01. *n* = 3–7 per group. EEC, enteroendocrine cell; NES, normalized enrichment score; RES, running enrichment score; RLM, ranked list metric.

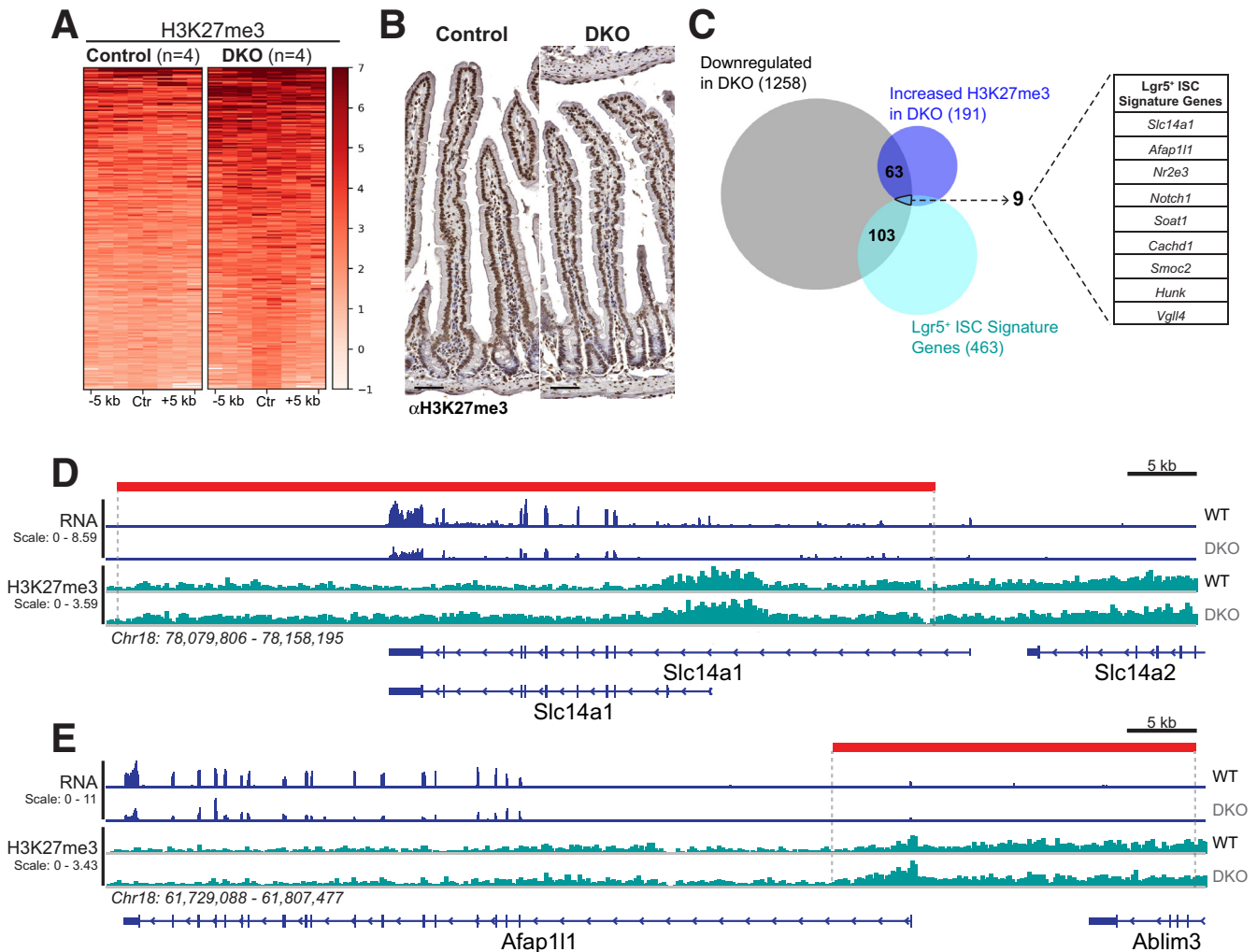


Figure 5. Differential gene expression after *Kdm6a/b* ablation is associated with modest changes in the H3K27me3 signal. (A) ChIP-seq for H3K27me3 in control and DKO mice after acute *Kdm6a/b* ablation. Heatmap of genomic regions with increased H3K27me3 levels in DKO mice. Genomic regions are shown in descending order based on mean H3K27me3 signal intensity in DKO mice. (B) Immunohistochemistry for H3K27me3 shows that acute *Kdm6a/b* ablation does not result in a global increase of H3K27me3 levels. Scale bars: 50 μ m. (C) Venn diagram showing overlap between genes down-regulated in DKO mice, genes associated with increased H3K27me3 in DKO mice, and genes falling into the Lgr5⁺ ISC gene signature. Overlap analysis was focused only on genes covered in both the ChIP-seq and RNA-seq analyses. A total of 72 genes were both down-regulated with an associated increase in H3K27me3 levels (expected overlap, 15; $P < 2.2e-16$ with the chi-square and Fisher exact tests). Right: Table lists the 9 genes belonging to the Lgr5⁺ ISC gene signature that are down-regulated with increased H3K27me3 levels in DKO mice. To identify the maximum possible overlap, no fold-change cut-off value was used when comparing the RNA-seq and ChIP-seq data. (D and E) IGV tracks of representative Lgr5⁺ ISC signature genes with decreased gene expression (blue tracks) and increased H3K27me3 levels (teal tracks) in DKO mice. Red bars represent genomic regions with statistically significant (FDR < 0.05) increases in H3K27me3 in DKO mice. n = 4 per group. Ctr, center of the genomic region; WT, wild type/controls.

H3K27 at enhancers.⁵⁹ Furthermore, in terminally differentiated human fibroblasts, KDM6A controls steady-state H3K27me3 levels at transcriptional start sites of *Hox* genes, suggesting a role for this enzyme in maintaining optimal H3K27me3 levels at genes that are maximally silenced in differentiated cells.^{17,60} In the intestinal epithelium, the master transcription factor caudal type homeobox 2 (CDX2) prevents H3K27me3 from spreading into vulnerable enhancer regions that are predisposed to H3K27me3 accumulation.^{61,62} KDM6A also binds these vulnerable

enhancers in a CDX2-dependent manner to help prevent H3K27me3 spreading and maintain accurate gene expression patterns.⁶² Thus, in intestinal epithelial cells, KDM6A and KDM6B may prevent the accumulation of H3K27me3 at vulnerable loci rather than directly activating gene expression during cellular transitions. Finally, reports of demethylase-independent functions of KDM6A and KDM6B leave open the possibility that both enzymes regulate the epigenomic environment of the intestinal epithelium via mechanisms that do not involve H3K27me3 removal.^{19,63}

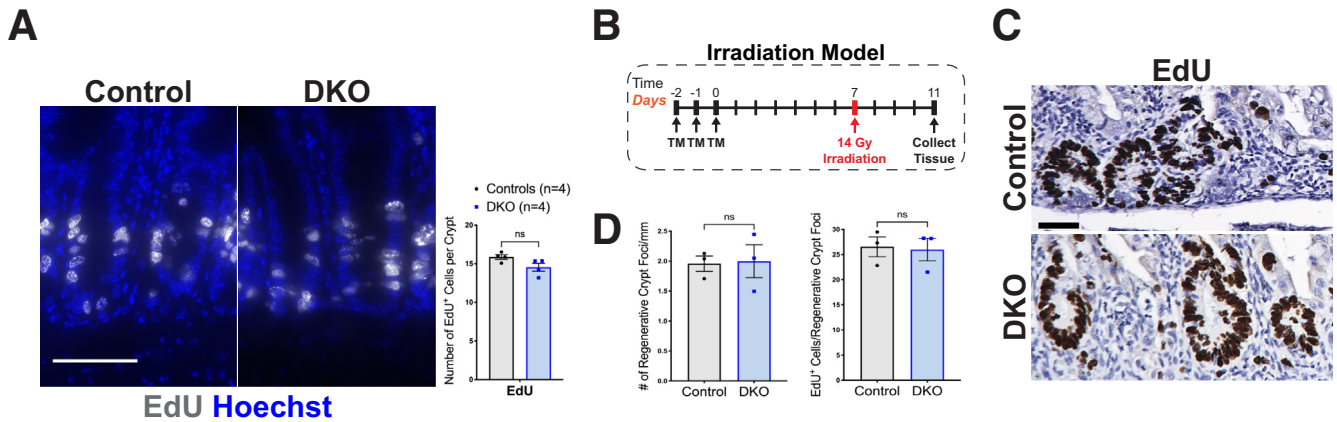


Figure 6. Intestinal epithelial cell renewal remains intact after acute *Kdm6a/b* ablation. (A) EdU incorporation in the proximal jejunum of control and DKO mice suggests that homeostatic cell renewal remains intact after acute *Kdm6a/b* ablation. Mice were injected with EdU 2 hours before being killed. $n = 4$ per group. Scale bar: 50 μm . (B) Experimental design for inducing radiation damage. Control and DKO mice were treated with daily tamoxifen (TM) injections for 3 consecutive days and then exposed to 14 Gy radiation 7 days later. Jejunum was collected 4 days after radiation treatment. (C) EdU incorporation into regenerative crypt foci of control and DKO mice 4 days after radiation treatment. EdU was injected into mice 2 hours before being killed. Scale bar: 50 μm . (D) Quantification of the number of regenerative crypt foci per millimeter (*left*) and number of EdU⁺ cells per regenerative crypt foci (*right*) show no statistically significant difference between control and DKO mice. $n = 3$ per group. EdU, 5-ethynyl-2'-deoxyuridine.

Our findings of modest gene expression and H3K27me3 changes after *Kdm6a/b* inactivation are consistent with previous studies investigating the chromatin landscape of the intestinal epithelium. Comparison of the repertoire of active intestinal enhancers in *Lgr5*⁺ ISCs, secretory progenitor cells, and enterocyte progenitor cells identified striking similarity among the cell populations, indicating that the *cis*-regulatory landscape of differentiating cells may be established already in *Lgr5*⁺ ISCs.^{6,10,33} Accordingly, comparison of *Lgr5*⁺ ISCs and intestinal villus cells found remarkably similar H3K27me3 patterns between both cell compartments and identified only a small fraction of genes that undergo H3K27me3 removal with associated transcriptional activation during the differentiation process.^{10,64} Thus, results from our study, together with these previous investigations of intestinal enhancer and H3K27me3 dynamics, support a model in which a permissive chromatin landscape exists within the intestinal epithelium: a chromatin landscape that does not require active H3K27me3 demethylation by KDM6A/B.

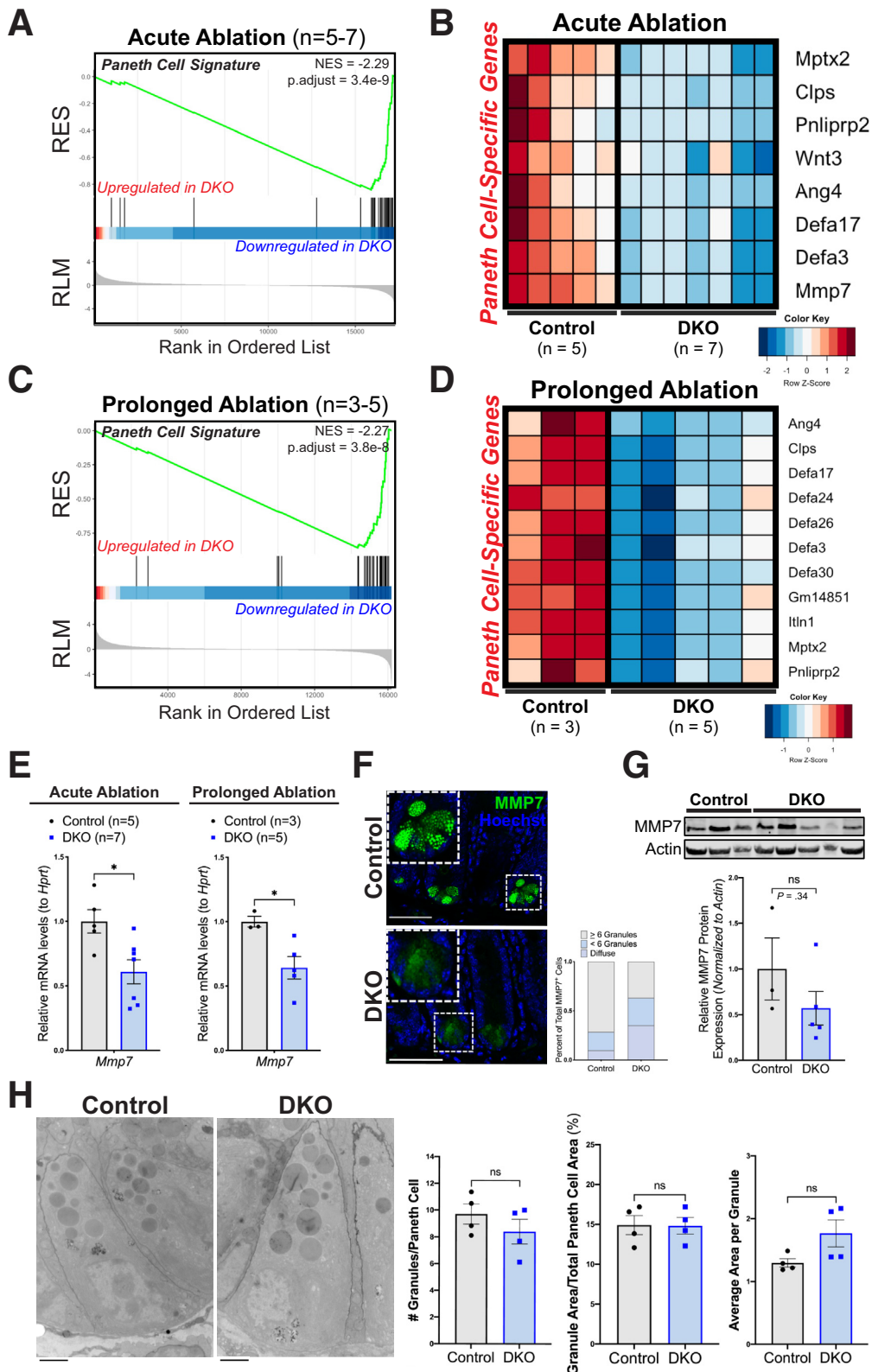
Importantly, significant changes in the distribution of H3K27me3 occur during the development of the embryonic intestinal epithelium into a mature adult organ.⁶⁴ A subset of enterocyte-specific genes lose H3K27me3 during the transition of embryonic intestinal progenitor cells into adult *Lgr5*⁺ ISCs, indicating that genes activated in enterocytes have lost H3K27me3 already in ISCs. Furthermore, a group of adult ISC signature genes, including *Smoc2* and *Notch1*, are marked with H3K27me3 in the intestinal epithelium at embryonic day 14.5, and lose this mark in adult ISCs.⁶⁴ Interestingly, we identified both *Smoc2* and *Notch1* as two dysregulated genes following *Kdm6a/b* ablation (Figure 4B), as both were down-regulated with a concomitant increase in

H3K27me3. Thus, it is possible that loss of *Kdm6a/b* predisposes genes that were developmentally marked with H3K27me3 to reaccumulate this repressive histone modification. Ultimately, these studies suggest that H3K27me3 patterns of the adult intestinal epithelium may be established during development and indicate that KDM6A/B may function in the embryonic intestinal epithelium to remove H3K27me3 or in the adult intestinal epithelium to maintain low H3K27me3 levels in developmentally marked genes.

Using the acute and prolonged ablation models to identify transcriptomic changes after *Kdm6a/b* depletion, we identified significant down-regulation of Paneth cell-specific genes, including genes encoding defensins and antimicrobial peptides. In addition, expression and localization of the defensin-processing enzyme, MMP7, was perturbed after prolonged *Kdm6a/b* ablation.^{47,65} Interestingly, we did not observe increased H3K27me3 levels at the *Mmp7* locus or at any other Paneth cell marker gene. Furthermore, analysis of H3K4me3 levels, a histone modification associated with active promoters and linked to KDM6A/B activity in certain contexts, did not identify differential patterns at Paneth cell gene promoters after *Kdm6a/b* ablation (data not shown).^{19,66–68} These findings are consistent with previous reports showing mild, demethylase-independent gene expression changes after *Kdm6b* inactivation,⁶⁶ and leave open the possibility that KDM6A/B use an alternative mechanism to regulate Paneth cell gene expression, for example, by promoting interactions between chromatin remodelers and transcription factors at enhancer elements.^{69,70} Furthermore, given current ChIP-seq limitations, we were unable to identify Paneth cell-specific changes in H3K27me3 levels after *Kdm6a/b* loss. To account for the high number of cells required for ChIP-seq, we used bulk,

crypt-enriched intestinal epithelial cells for our analysis of H3K27me3 patterns after *Kdm6a/b* ablation. Thus, it remains possible that KDM6A/B have cell type-specific

demethylase functions that are obscured when analyzing H3K27me3 patterns in bulk intestinal epithelial cells. With the anticipated development of new technologies



enabling ChIP-seq at single-cell resolution, it would be interesting to revisit cell type-specific H3K27me3 dynamics, specifically within the Paneth cell population, after *Kdm6a/b* ablation.⁷¹

There were several limitations to the current study. First, although we ablated both *Kdm6a* and *Kdm6b* simultaneously with the goal of removing all H3K27me3 demethylase activity, the possibility remains that an as yet unidentified demethylase compensates for *Kdm6a/b* removal and facilitates H3K27me3 demethylation in their absence. Second, evidence that KDM6A/B can localize both to the nucleus and cytoplasm,^{72,73} together with our findings of disrupted MMP7 localization after prolonged *Kdm6a/b* loss, raises the possibility that these enzymes have unknown cytoplasmic function in regulating protein localization to Paneth cell secretory granules. Finally, given the evidence of extensive H3K27me3 changes during intestinal development, it remains possible that KDM6A/B functions in fetal development to promote the differentiation of embryonic intestinal progenitor cells into adult intestinal epithelial cells.⁶⁴ Additional studies using an intestine-specific, developmental *Kdm6a/b* gene ablation mouse model would be needed to address this possibility.

In sum, our study shows limited involvement of KDM6A/B in regulating intestinal homeostasis. When taken together with our understanding of the epigenetic landscape of the intestine, both during development and in the adult, we can appreciate the limited role for H3K27me3 removal in driving cellular differentiation in the established intestinal epithelium. Despite the modest function of KDM6A/B in the intestine, our findings enhance our overall comprehension of the epigenetic mechanisms regulating intestinal biology and complement previous studies identifying replicational dilution as the dominant mechanism regulating H3K27me3 removal in the intestinal epithelium.

Materials and Methods

Mouse Studies

All animal experiments performed in this study were reviewed and approved by the Institutional Animal Care and Use Committee of the Office of Animal Welfare at the University of Pennsylvania. Mice were subjected to 12-hour

light-dark cycles, fed standard rodent chow, and had access to water at all times. Two- to 7-month-old female mice were used for all experiments. *Kdm6a^{fl/fl}* mice have been described previously¹⁹ and were re-derived in the University of Pennsylvania Transgenic and Chimera Mouse Facility using the *Kdm6a* JM8A3.N1 GO1 embryonic stem cell line. *Kdm6b^{fl/fl}* and *Villin-Cre^{ERT2}* mice were generously donated by Dr Giuseppe Testa and Dr Sylvie Robine, respectively.

To induce Cre activity, animals were treated by intraperitoneal injection with 1.6 mg/30 g body weight of tamoxifen (T5648; Sigma-Aldrich) dissolved in sunflower seed oil. Animals were injected with tamoxifen once daily for 3 consecutive days and killed 7 days after the final tamoxifen dose. To induce prolonged *Kdm6a* and *Kdm6b* ablation, mice were treated for 3 consecutive days with tamoxifen as described earlier and killed 5 months after the final tamoxifen dose.

For the EdU incorporation assay, mice were treated by intraperitoneal injection with 150 mL of 10 mg/mL EdU (C10640; Invitrogen) dissolved in water 2 hours before being killed.

Radiation studies were completed at the University of Pennsylvania Small Animal Radiation Research Platform. Mice were anesthetized using 2% isoflurane and subsequently treated with a single dose of 14 Gy 220 keV X-rays to the whole body. A shield was used to protect the head and neck of mice. Mice were monitored daily after irradiation treatment until the experimental end point.

Histology, Immunohistochemistry, and Transmission Electron Microscopy

The small intestine was isolated and the proximal 2 cm discarded as duodenum. The next proximal 4–7 cm was isolated as proximal jejunum, cut longitudinally, and rinsed in cold phosphate-buffered saline (PBS). For ileum studies, the distal-most 6 cm of the small intestine was collected. Intestinal tissue was made into a Swiss Roll, fixed in 4% paraformaldehyde overnight at 4°C, embedded in paraffin, and sectioned.

Tissue sections were deparaffinized with xylene and rehydrated by serial incubation of 100%, 95%, 80%, and 70% ethanol followed by PBS. Antigen retrieval was

Figure 7. KDM6A and KDM6B regulate expression of the Paneth cell gene signature. GSEA plots showing down-regulation of the Paneth cell gene signature after (A) acute and (C) prolonged *Kdm6a/b* ablation. Heatmap representation of Paneth cell-specific genes that are down-regulated in DKO mice after (B) acute and (D) prolonged *Kdm6a/b* ablation. Down-regulated Paneth cell-specific genes include multiple antimicrobial peptides and defensins. *n* = 3–7 per group. (E) RT-qPCR analysis confirms down-regulation of *Mmp7* mRNA after acute and prolonged *Kdm6a/b* ablation. *n* = 3–7 per group. **P* < .05. (F) Immunohistochemistry of MMP7 in control and DKO mice after prolonged *Kdm6a/b* ablation. Right: Quantifications of the percentage of the total MMP7⁺ cell population belonging to each of 3 categories: diffuse, <6 granules, and ≥6 granules. MMP7 typically localizes to Paneth cell granules but adopts a diffuse staining pattern after prolonged *Kdm6a/b* ablation. Dashed white boxes depict zoomed-in crypt regions. Statistical analysis was performed using the chi-square test for independence: χ^2 (degrees of freedom = 2, *n* = 7–9) = 157.8, *P* < .0001. *n* = 7–9 per group. Scale bars: 50 μ m. (G) Western blot analysis shows a trend toward decreased MMP7 protein levels after prolonged *Kdm6a/b* ablation. MMP7 expression levels were normalized to actin. *n* = 3–5 per group. (H) Transmission electron microscopy of electron-dense Paneth cell secretory granules in control and DKO mice after prolonged *Kdm6a/b* ablation. Right: Quantifications showing no significant difference between control and DKO mice when measuring the number of granules per Paneth cell, the percentage area of each Paneth cell occupied by granules, and the average granule area. *n* = 4 per group. Scale bars: 2 μ m. Statistical comparisons were made using the Student's *t* test with Welch's correction except where otherwise noted. NES, normalized enrichment score; RES, running enrichment score; RLM, ranked list metric.

performed in citric acid buffer (10 mmol/L citric acid, 0.05% Tween 20, pH 6.0) or Tris-EDTA-Tween buffer (10 mmol/L Tris base, 1 mmol/L EDTA, 0.05% Tween 20, pH 9.0) in a pressure cooker (2100 Antigen Retriever; Aptum Biologics, Ltd) and the slides cooled to room temperature. Slides then were blocked with blocking buffer (008120, CAS-Block; Invitrogen) for 30 minutes followed by overnight incubation of primary antibodies diluted in blocking buffer at 4°C in a humidified chamber. To detect EdU signal, tissue sections were incubated in Click-iT Edu Reaction Cocktail for 30 minutes at room temperature before blocking and primary antibody incubation (C10640; Invitrogen). The next day, 3 washes of PBS were performed followed by incubation with secondary antibodies at room temperature for 2 hours. Rabbit anti-ubiquitously transcribed tetra-ricopeptide repeat gene X chromosome (33510S, 1:150; Cell Signaling), rabbit anti-chromogranin A (20085, 1:1000; Immunostar), rabbit antilysozyme (A0099, 1:1000; Dako), rat anti-Ki-67 (50-245-563, 1:500; Invitrogen), rabbit anti-MMP7 (3801S, 1:100; Cell Signaling), and mouse anti-E-cadherin (610181, 1:500; BD Biosciences) primary antibodies were used. Secondary antibodies included Cy3 anti-mouse, Cy3 anti-rabbit, Cy2 anti-mouse, and Cy2 anti-rabbit antibodies. Hoechst dye (H3570, 1:10,000; Molecular Probes) was used to label nuclei.

For colorimetric staining, tissue sections were deparaffinized and endogenous peroxidase enzymes were quenched in 3% hydrogen peroxide (426000250; Thermo Scientific). Slides were sequentially blocked in Avidin D blocking reagent, biotin blocking reagent, and Cas Block (SP-2001; Vector Laboratories). The tissue sections then were incubated overnight in primary antibodies diluted in Cas Block. The following day, the tissue sections were washed and incubated in biotinylated secondary antibodies for 1 hour followed by an incubation with horseradish-peroxidase-conjugated avidin (PK-7100; Vector Laboratories). Antibody signal was developed by incubating the tissue sections with 3,3'-diaminobenzidine tetra hydrochloride substrate (SK-4100; Vector Laboratories). The tissue sections were washed, counterstained with hematoxylin, dehydrated, and mounted (H-5000-60; Vector Laboratories). Primary antibodies included rabbit anti-H3K27me3 (07-449, 1:500; Millipore Sigma), and secondary antibodies included goat anti-rabbit IgG biotinylated antibody (BA-1000-1.5; Vector Laboratories). For colorimetric EdU staining, the earlier-described protocol was followed with slight modifications in accordance with the manufacturer's protocol (C10644; Invitrogen). After deparaffinization and quenching, antigen retrieval was completed using a trypsin-EDTA solution. Tissue sections then were treated with the Click-iT Edu Reaction cocktail for 30 minutes, followed by a 15-minute wash in 1× Click-iT Edu Wash Buffer and a 30-minute incubation with streptavidin-peroxidase conjugate. EdU signal subsequently was developed, and tissue sections were counterstained and mounted.

To visualize goblet cells, deparaffinized and rehydrated tissue sections were stained in Alcian blue solution (Alcian blue 8GX, 3% acetic acid, pH 2.5) for 30 minutes, washed in running tap water for 2 minutes, and counterstained with

hematoxylin. Tissue sections then were dehydrated, cleared in xylene, and mounted.

Brightfield and fluorescent images were obtained using a Keyence BZ-X700 microscope, a Keyence BZ-X800 microscope, and a Leica laser scanning confocal microscope (TCS SP8; Penn Cell and Developmental Biology Microscopy Core). Images were processed and brightness and contrast were enhanced using FIJI (ImageJ, version 2.1.0; National Institutes of Health) or Keyence Analysis Software.

Samples for transmission electron microscopy analysis were collected from the proximal jejunum. Briefly, the small intestine was isolated and the proximal 2 cm of the intestine was discarded. The next 2 cm of proximal intestine was collected, cut into four 3- to 4-mm pieces, rinsed in electron microscopy fixative (2.5% glutaraldehyde, 2.0% paraformaldehyde in 0.1 mol/L sodium cacodylate buffer, pH 7.4), and incubated in fixative for approximately 48 hours at 4°C. After subsequent buffer washes, the samples were postfixed in 2.0% osmium tetroxide for 1 hour at room temperature and rinsed in deionized H₂O before en bloc staining with 2% uranyl acetate. After dehydration through a graded ethanol series, the tissue was infiltrated and embedded in EMBED-812 (Electron Microscopy Sciences, Fort Washington, PA). Thin sections were stained with uranyl acetate and lead citrate and then examined with a JEOL 1010 electron microscope fitted with a Hamamatsu digital camera and AMT Advantage image capture software.

Data are presented as means ± SEM. Only well-positioned crypts were quantified. For immunohistochemical analysis, at least 16 crypts were analyzed per biological replicate. For transmission electron microscopy analysis, at least 6 Paneth cells identified by the presence of electron-dense granules were analyzed per biological replicate. Statistical differences between groups were assessed by the Student *t* test with Welch correction, the Mann-Whitney test with corrections for multiple comparisons by controlling false discovery rate (FDR), or by a chi-square test of independence, as appropriate. Statistical analyses were performed using GraphPad Prism software (9.0.1; GraphPad Software, LLC).

RNA Extraction, RT-qPCR, and RNA-Seq

The small intestine from stomach to cecum was dissected, and the first 4 cm was discarded as duodenum. The proximal jejunum, measured as the next one third of the small intestine, was cut longitudinally, rinsed 3 times in ice-cold PBS, and washed for 10 minutes in dissociation buffer (PBS pH 8.0, 5 mmol/L EDTA) at 4°C with rotation. The tissue was placed in fresh dissociation buffer (PBS pH 8.0, 5 mmol/L EDTA) and incubated for 40 minutes at 4°C with rotation. Intestinal epithelial cells were mechanically dissociated from the underlying mesenchyme by shaking vigorously for approximately 30 seconds every 10 minutes during the incubation period. The solid tissue then was discarded, and the supernatant containing intestinal epithelial cells was filtered using a 70-mm cell strainer (352350; Corning Falcon) to enrich for crypts. The filtrate was centrifuged for 5 minutes at 300 × *g* at 4°C and washed once with ice-cold PBS. Sedimented intestinal epithelial cells

then were resuspended in 2 mL TRIzol reagent (15596026; Invitrogen) and stored at -80°C until RNA extraction.

RNA was extracted using the RNeasy Micro Kit (74004; QIAGEN) following the manufacturer's protocol. Briefly, intestinal epithelial cells lysed in TRIzol reagent (15596026; Invitrogen) were treated with chloroform to denature proteins and extract RNA. After a 10-minute centrifugation at 4°C ($17,000 \times g$), the aqueous phase containing RNA was isolated, washed, eluted in RNase-free water, and quantified using the NanoDrop 1000 Spectrophotometer (Thermo Fisher) and BioAnalyzer RNA 6000 Nano (5067-1511; Agilent) systems. Samples with an RNA integrity number of 7 or greater were used for downstream analysis.

After RNA extraction, complementary DNA synthesis was performed using the SuperScript II Reverse Transcriptase system (18064022; Invitrogen). An input of 500 ng of RNA for each sample was used for complementary DNA synthesis. RT-qPCR was completed using the Brilliant III Ultra-Fast SYBR Green qPCR system with ROX reference dye (600883; Agilent Technologies). Reactions were run on an Agilent Stratagene MX3005P qPCR system and fold changes were calculated using the delta-delta-cycle threshold (ddCt) method with *ActinB* and *Hprt* as internal controls. The following primer sequences were used: *Actb* forward: 5'-GAAGTGTGACGTTGACATCCG-3', *Actb* reverse: 5'-GTCAGCAATGCCTGGGTACAT-3'; *Hprt* forward: 5'-GGTTAAGCAGTACAGCCCCA-3', *Hprt* reverse: 5'-GGCCTGTATCCAACACTTCG-3'; *Kdm6a* forward: 5'-TTCGGGTTTCGTGAGGTTTCA-3', *Kdm6a* reverse: 5'-CGTAGCAGCGAA CAGCCTTG-3'; *Kdm6b* forward: 5'-ACAGTCCACTTCCA ACTCCATC-3', *Kdm6b* reverse: 5'-TCCACAGAAAAG-CCAAT-CATCA-3'; *Ncald* forward: 5'-GGCAGAAATGCTGGAGATTG-3', *Ncald* reverse: 5'-TATTGGTATCCATCTGGCGG-3'; *Slc6a20b* forward: 5'-GTACCAAGCCTGGGATGCTACTCA-3', *Slc6a20b* reverse: 5'-CTGATCTTGAAGTGGCGTGTGACA-3'; *Epb4111* forward: 5'-GGACACCCACCAAGATCAAG-3', *Epb4111* reverse: 5'-GCCTGGTCTTCAACAAGAC-3'; *Dclk3* forward: 5'-TTACTGTGTGTGGGACGCC-3', *Dclk3* reverse: 5'-GGAAGCCACA-CAAGAGGATG-3'; *Paqr5* forward: 5'-GGCTATTCCGCATAGACCAG-3', *Paqr5* reverse: 5'-CGTCCAGATGTTGA-GGG TCT-3'; *Akr1c14* forward: 5'-TGTGGTCTGACCAGGAGT T-3', *Akr1c14* reverse: 5'-GTCCTCTGAAGCCAACTGGA-3'; *Afap111* forward: 5'-CCCCGAGTATATCAGCTCTC-3', *Afap111* reverse: 5'-GGTGGGGTAGCTGTTGTCTG-3'; *Slc14a1* forward: 5'-GGAGGGATGTTTCATGGCACT-3', *Slc14a1* reverse: 5'-GG TACAAGCTGGCAGGTGAA-3'; *Reg4* forward: 5'-AACC-TGCCTGTGTGGATTGG-3', *Reg4* reverse: 5'-GTTTCATCTCAG CGCAATGCC-3'; *Mptx2* forward: 5'-AGGAAGTGTAGCACAAA-CAGACAT-3', *Mptx2* reverse: 5'-TGTCCTTAGT-TCTTGTGCTG TAGG-3'; *Cdx1* forward: 5'-GGACGCCCTACGAATGGAT-3', *Cdx1* reverse: 5'-TGTCCTTGGTTCGGGTCTTA-3'; *Ccnd3* forward: 5'-CCTCCTACTTCCAGTGCCTG-3', *Ccnd3* reverse: 5'-AGCCAGAGGGAAGACATCCT-3'; and *Mmp7* forward: 5'-GGCT TCGCAAGGAGAGATCA-3', *Mmp7* reverse: 5'-GCCAAATTCA TGGGTGGCAG-3'.

RNA-seq libraries were prepared using the NEBNext Ultra RNA Library Prep Kit from Illumina (E7530; NEB) with the NEBNext Poly(A) mRNA Magnetic Isolation Module (E7490; NEB). An input of 250 ng RNA was used for each

sample, and manufacturer protocols were followed at all library preparation steps. NEBNext Multiplex Oligos for Illumina (E7730; NEB) were used as index primers for library multiplexing, and DNA purification was completed using Agencourt AMPure XP Beads (A63881; Beckman Coulter). Library concentrations were measured using the Qubit dsDNA High Sensitivity Assay Kit (Q32854; Thermo Fisher), and library quality was assessed using a BioAnalyzer High Sensitivity DNA Analysis (5067-4626; Agilent) system. DNA libraries were sequenced on an Illumina NovaSeq 6000 with 100 base pair single-end reads.

RNA-seq data quality was assessed using the FastQC program (v0.11.5). Alignment against the mm9 reference genome was performed using the STAR method (v2.4.0) with default parameters and a maximum fragment size of 2 kb. Samtools (v1.9) then was used to filter for properly paired primary alignments. Mitochondrial reads and reads on nonchromosome contigs were removed using Bedtools (v2.27.1), and read counts on RefSeq genes were computed using featureCounts (v1.6.2) in the nonstranded manner. Differential gene expression analysis was performed using the DESeq2⁷⁴ (Bioconductor) R package with normalization to correct for library sizes. We define genes as differentially expressed genes with an FDR value of 0.05 or less.

GSEA was performed using the GSEABase (1.52.1) and clusterProfiler (3.18.1) packages in R (4.0.4). GSEA enrichment plots were produced using the enrichplot package (1.10.2). Intestinal cell type-gene signatures were obtained from published resources.³²⁻³⁵ A total of 9 intestinal cell type signatures were used as input for GSEA analysis, and the genes making up the Paneth cell gene signature were cross-validated across 2 different data sets to ensure accuracy.^{32,34} Volcano plots and bubble plots were generated using the tidyverse ggplot2 package (1.3.0), and heatmaps were produced using the heatmap.2 function in the gplots package (3.1.1). To visualize RNA-seq genome tracks, the CrossMap (v0.6.1) program in python (v3.9.1) was used to liftover the mm9 bigWig files to the mm10 genome build. Genome tracks then were produced of the mm10 build bigWig files using the IGV (v2.11.9). Venn diagrams were produced using the BioVenn web application.⁷⁵

Chromatin Isolation and ChIP-Seq

The entire small intestine was removed, and the proximal 2 cm was discarded as duodenum. The next 4 cm of tissue was collected for histology, and the next one third of intestine was collected as the proximal jejunum and cut open longitudinally. Jejunal intestinal epithelial cells were dissociated as described earlier and subsequently fixed by incubation in 1% paraformaldehyde for 15 minutes with rotation at room temperature. To quench paraformaldehyde, the cells were treated with 0.125 mol/L glycine for 5 minutes with rotation at room temperature. Fixed cells then were washed twice using PBS supplemented with EDTA-free protease inhibitor (4693132001; Sigma-Aldrich). The washed and fixed cells were lysed and MNase-digested immediately or flash frozen and stored at -80°C for later processing.

To digest isolated chromatin, a 10-U/mL and a 5-U/mL MNase (LS004797; Worthington) solution was prepared in cell lysis buffer (150 mmol/L NaCl, 50 mmol/L Tris-HCl pH

8.0, 1% Triton X-100 (T8787, Sigma-Aldrich), 0.1% deoxycholic acid sodium salt (DOC), 5 mmol/L CaCl_2) supplemented with EDTA-free protease inhibitor (4693132001; Sigma-Aldrich). Fixed cells were resuspended in cell lysis buffer and subsequently treated with 2 mL of 10 U/mL or 5 U/mL MNase for a final amount of 20 U and 10 U MNase, respectively. Cell lysis then was completed by incubating the cells for 15 minutes on ice with occasional physical agitation. MNase activity subsequently was induced by incubating the lysed cells at 37°C for 10 minutes. To quench MNase activity, 20 mmol/L EDTA was added, and the digested chromatin solution was incubated on ice for 10 minutes. Samples then were centrifuged ($17,000 \times g$, 10 minutes, 4°C) and the supernatant was removed and placed in a fresh tube. Digested chromatin then was evaluated for quality (as described later) or stored at -80°C for later ChIP-seq library preparation.

To evaluate the product of MNase digestion, 10 mL digested chromatin was removed to a fresh tube and treated with 1 mL of 10 mg/mL RNase A for 30 minutes at 37°C. Then, 40 mL Proteinase K solution (10 mmol/L Tris-HCl pH 8.0, 5 mmol/L EDTA, 300 mmol/L NaCl, 0.6% sodium dodecyl sulfate [SDS], and 50 U Proteinase K) was added and the sample was incubated at 37°C for 2 hours, followed by a 16-hour incubation step at 65°C. DNA was purified using 2× Agencourt AMPure XP Beads (A63881; Beckman Coulter) and resuspended in 20 mL elution buffer (10 mmol/L Tris-HCl, pH 8.0). DNA concentration was measured using the Qubit dsDNA High Sensitivity Assay Kit (Q32854; Thermo Fisher), and DNA quality was visualized using a BioAnalyzer High Sensitivity DNA Analysis (5067-4626; Agilent) system.

ChIP-seq libraries were prepared as previously described with the following modifications.⁷⁶ Digested chromatin samples were combined (20 U and 10 U samples) and incubated with 2 mg H3K27me3 antibody (07-449; Millipore Sigma) overnight at 4°C with rotation. The next day, 20 mL Protein G Dynabeads (10004D; Thermo Fisher) per sample were washed 3 times with ice-cold cell lysis buffer (150 mmol/L NaCl, 50 mmol/L Tris-HCl pH 8.0, 1% Triton X-100, 0.1% DOC, 5 mmol/L CaCl_2) and resuspended in an equal volume of cell lysis buffer supplemented with EDTA-free protease inhibitor (4693132001; Sigma-Aldrich). Samples were spun down and incubated with 20 mL washed beads for 1 hour with rotation at 4°C. Samples then were washed 5 times with RIPA buffer (10 mmol/L Tris-HCl pH 8.0, 140 mmol/L NaCl, 1 mmol/L EDTA, 0.1% SDS, 0.1% DOC, 1% Triton X-100), 3 times with RIPA-500 buffer (10 mmol/L Tris-HCl pH 8.0, 500 mmol/L NaCl, 1 mmol/L EDTA, 0.1% SDS, 0.1% DOC, 1% Triton X-100), 3 times with lithium chloride (LiCl) wash buffer (10 mmol/L Tris-HCl pH 8.0, 0.25 mol/L LiCl, 1 mmol/L EDTA, 0.5% DOC, 0.5% IGEPAL CA-630 [I8896-50ML; Sigma-Aldrich]), and 3 times with 10 mmol/L Tris-HCl, pH 7.4. All washes were completed in a volume of 150 mL using ice-cold buffers.

Next, end repair was completed by resuspending the chromatin bead complex in 10 mL of 10 mmol/L Tris-HCl pH 7.4 supplemented with EDTA-free protease inhibitor. The samples then were treated with 15 mL ER mix (50 mmol/L Tris-HCl pH 7.5, 10 mmol/L MgCl_2 , 10 mmol/L dithiothreitol,

1 mmol/L adenosine triphosphate, 0.4 mmol/L each deoxynucleoside triphosphate, 0.15 U/mL PNK, 0.04 U/mL T4 Pol, protease inhibitor) and incubated at 12°C for 22 minutes, followed by a 22-minute incubation at 25°C. Samples were washed twice in 150 mL elution buffer (10 mmol/L Tris-HCl pH 8.0) and resuspended in 20 mL elution buffer (10 mmol/L Tris-HCl pH 8.0) supplemented with EDTA-free protease inhibitor. dA tailing was completed by adding 10 Deoxyadenosine monophosphate mL dA mix (2.83 mmol/L Tris-HCl pH 8.0, 2.83 mmol/L MgCl_2 , 14.2 mmol/L NaCl, 0.28 mmol/L dithiothreitol, 0.16 mmol/L dATP, 0.25 U/mL Klenow Exo) to each sample and incubating the samples for 30 minutes at 37°C. Samples were again washed once with elution buffer (10 mmol/L Tris-HCl pH 8.0) and resuspended in 9 mL elution buffer (10 mmol/L Tris-HCl pH 8.0) supplemented with EDTA-free protease inhibitor.

Adaptor ligation was completed by adding 2.5 mL TruSeq RNA Single Index adaptors (15032612, 15032613; Illumina) and 17 mL Adaptor Ligation Master Mix (14.5 mL 2× Quick Ligation Buffer [M2200S, New England Biolabs], 2.5 mL DNA Quick Ligase) to each sample. Samples were incubated for 45 minutes at 25°C and washed 3 times with RIPA buffer (10 mmol/L Tris-HCl pH 8.0, 140 mmol/L NaCl, 1 mmol/L EDTA, 0.1% SDS, 0.1% DOC, 1% Triton X-100), once with RIPA-500 buffer (10 mmol/L Tris-HCl pH 8.0, 500 mmol/L NaCl, 1 mmol/L EDTA, 0.1% SDS, 0.1% DOC, 1% Triton X-100), and once with LiCl Wash Buffer (10 mmol/L Tris-HCl pH 8.0, 0.25 mol/L LiCl, 1 mmol/L EDTA, 0.5% DOC, 0.5% IGEPAL). Reverse cross-linking was completed by incubating samples in 24 mL Elution Buffer with SDS (10 mmol/L Tris-HCl pH 8.0, 5 mmol/L EDTA, 300 mmol/L NaCl, 0.6% SDS) supplemented with 1 mL of 10 mg/mL RNase A for 30 minutes at 37°C. Samples then were treated with 24 mL Elution Buffer with SDS (10 mmol/L Tris-HCl pH 8.0, 5 mmol/L EDTA, 300 mmol/L NaCl, 0.6% SDS) supplemented with 1 mL Proteinase K and incubated for 2 hours at 37°C followed by a 16-hour incubation at 65°C.

Reverse cross-linked DNA was purified using 0.85× Agencourt AMPure XP Beads (A63881; Beckman Coulter) and eluted in 25 mL elution buffer (10 mmol/L Tris-HCl, pH 8.0). Libraries then were PCR amplified using the Kapa HiFi HotStart ReadyMix (07958935001; Roche) and the TruSeq DNA Sample Preparation PCR Primer Cocktail (15031748; Illumina). After amplification, DNA libraries were purified using 0.85× Agencourt AMPure XP beads to yield the final ChIP-seq libraries. Library concentrations were measured using the Qubit dsDNA High Sensitivity Assay Kit (Q32854; Thermo Fisher), and library quality was visualized using a BioAnalyzer High Sensitivity DNA Analysis (5067-4626; Agilent) system. ChIP-seq libraries were run on an Illumina NovaSeq 6000 with 50 base pair paired-end reads.

ChIP-seq data quality was assessed using FastQC (v0.10.1), and raw read alignment to the mm10 reference genome was completed using Bowtie (v0.12.7). Aligned reads were filtered using samtools (v1.11) and picard (v1.141) to remove reads that were unmapped, reads in which the next segment was unmapped, reads that were not aligned properly, reads not passing platform quality, secondary alignments, and PCR or optical duplicates. Deduplication was performed using picard (v1.141). Peak calling using SICER2 (v1.0.3) was performed on

the filtered, sorted, deduplicated bam files, and wig files were produced to visualize coverage generated by peak calling.⁷⁷ Differential methylation analysis was performed using csaw^{78,79} to directly identify quantitative changes in the H3K27me3 profiles between the control and DKO conditions. Reads overlapping the ENCODE blacklisted regions were removed. Reads then were counted using 2 different sliding window resolutions (2000 bp with 500 bp spacing and 1000 bp with 250 bp spacing), and windows having at least 2-fold more coverage than the average background (estimated using 10-kb bins) were retained. Normalization factors were computed using the composition bias method, and edgeR was used for statistical modeling of differential H3K27me3. Combined *P* values for the 2 window resolutions were calculated by csaw using the Simes' method for region-level FDR control.^{79,80} All regions with an FDR less than 0.05 were called differentially methylated. Differentially methylated regions were annotated to all neighboring genes within 5000 base pairs of the region. Annotation leveraged the following Bioconductor R packages: TxDb.Mmusculus.UCSC.mm10.knownGene and org.Mm.eg.db.

ChIP-seq heatmaps were produced using the deepTools (v3.5.1) computeMatrix and plotHeatmap functions. Genomic regions with increased H3K27me3 in DKO mice were used as the input regions and the center reference point setting was used. Genomic regions were sorted based on decreasing mean signal intensity in DKO mice. ChIP-seq genome tracks were produced using IGV (v2.11.9).

Western Blot

Tissue samples were collected after prolonged *Kdm6a/b* ablation. A 1-cm region of the proximal jejunum was removed, rinsed in ice-cold PBS, and snap-frozen in liquid nitrogen. Tissue samples were stored at -80°C until analysis. Western blot was performed as previously described, with slight modifications.⁸¹ Briefly, protein extracts were prepared from frozen tissue by placing tissue in RIPA buffer with protease inhibitors (Roche), followed by sonication using a Diagenode Bioruptor for 7 minutes (30 seconds on, 30 seconds off, high setting). Protein was quantified using a standard BCA assay (Pierce). Proteins were separated in 4%–12% Bis-Tris NuPAGE gels (Invitrogen) and transferred to a nitrocellulose membrane using a Bio-Rad Transblot Turbo system. The membrane was blocked with Intercept blocking buffer (TBS, LI-COR) for 1 hour and then overnight with primary antibodies. Antibodies used were as follows: rabbit anti-Mmp7 (1:1000, cat# 2443S, RRID:AB_823598; Cell Signaling) and mouse anti-actin (1:10,000, clone C4, MAB1501; Millipore). After washing, blots were incubated with the following secondary antibodies: anti-mouse IgG IRDye 680RD (cat# 926-68072, RRID:AB_10953628; LI-COR) and anti-rabbit IgG, donkey, IRDye 800CW (cat# 926-32213, RRID:AB_621848; LI-COR). Blots were imaged on a LI-COR Odyssey imaging system.

Access to Data

All authors had access to the study data and reviewed and approved the final manuscript. The data sets generated during this study are available in the Gene Expression Omnibus Database: GSE200976.

References

1. Barker N, Van Es JH, Kuipers J, et al. Identification of stem cells in small intestine and colon by marker gene *Lgr5*. *Nature* 2007;449:1003–1007.
2. Cheng H, Leblond CP. Origin, differentiation and renewal of the four main epithelial cell types in the mouse small intestine I. Columnar cell. *Am J Anat* 1974; 141:537–562.
3. Snippert HJ, van der Flier LG, Sato T, et al. Intestinal crypt homeostasis results from neutral competition between symmetrically dividing *Lgr5* stem cells. *Cell* 2010; 143:134–144.
4. Lopez-Garcia C, Klein AM, Simons BD, Winton DJ. Intestinal stem cell replacement follows a pattern of neutral drift. *Science* 2010;330:822–825.
5. Yousefi M, Li L, Lengner CJ. Hierarchy and plasticity in the intestinal stem cell compartment. *Trends Cell Biol* 2017;27:753–764.
6. Verzi MP, Shivdasani RA. Epigenetic regulation of intestinal stem cell differentiation. *Am J Physiol Gastrointest Liver Physiol* 2020;319:189–196.
7. Bracken AP, Dietrich N, Pasini D, et al. Genome-wide mapping of polycomb target genes unravels their roles in cell fate transitions. *Genes Dev* 2006;20:1123–1136.
8. Chammas P, Mocavini I, Di Croce L. Engaging chromatin: PRC2 structure meets function. *Br J Cancer* 2020; 122:315–328.
9. Margueron R, Reinberg D. The Polycomb complex PRC2 and its mark in life. *Nature* 2011;469:343–349.
10. Jadhav U, Nalapareddy K, Saxena M, et al. Acquired tissue-specific promoter bivalency is a basis for PRC2 necessity in adult cells. *Cell* 2016;165:1389–1400.
11. Koppens MAJ, Bounova G, Gargiulo G, et al. Deletion of polycomb repressive complex 2 from mouse intestine causes loss of stem cells. *Gastroenterology* 2016;151:684–697.e12.
12. Chiacchiera F, Rossi A, Jammula S, et al. PRC2 preserves intestinal progenitors and restricts secretory lineage commitment. *EMBO J* 2016;35:2301–2314.
13. Nakanishi Y, Reina-Campos M, Nakanishi N, et al. Control of Paneth cell fate, intestinal inflammation, and tumorigenesis by *PKC λ /i*. *Cell Rep* 2016;16:3297–3310.
14. Agger K, Cloos PAC, Christensen J, et al. UTX and JMJD3 are histone H3K27 demethylases involved in HOX gene regulation and development. *Nature* 2007;449:731–734.
15. Lee MG, Villa R, Trojer P, et al. Demethylation of H3K27 regulates polycomb recruitment and H2A ubiquitination. *Science* 2007;318:447–450.
16. De Santa F, Totaro MG, Prosperini E, et al. The histone H3 lysine-27 demethylase *Jmjd3* links inflammation to inhibition of polycomb-mediated gene silencing. *Cell* 2007;130:1083–1094.
17. Lan F, Bayliss PE, Rinn JL, et al. A histone H3 lysine 27 demethylase regulates animal posterior development. *Nature* 2007;449:689–694.
18. Greenfield A, Carrel L, Pennisi D, et al. The UTX gene escapes X inactivation in mice and humans. *Hum Mol Genet* 1998;7:737–742.
19. Shpargel KB, Sengoku T, Yokoyama S, Magnuson T. UTX and UTY demonstrate histone demethylase-

- independent function in mouse embryonic development. *PLoS Genet* 2012;8:e1002964.
20. Walport LJ, Hopkinson RJ, Vollmar M, et al. Human UTY(KDM6C) is a male-specific N^ε-methyl lysyl demethylase. *J Biol Chem* 2014;289:18302–18313.
 21. Welstead GG, Creighton MP, Bilodeau S, et al. X-linked H3K27me3 demethylase Utx is required for embryonic development in a sex-specific manner. *Proc Natl Acad Sci U S A* 2012;109:13004–13009.
 22. Dhar SS, Lee S-H, Chen K, et al. An essential role for UTX in resolution and activation of bivalent promoters. *Nucleic Acids Res* 2016;44:3659–3674.
 23. Liu J, Mercher T, Scholl C, et al. A functional role for the histone demethylase UTX in normal and malignant hematopoietic cells. *Exp Hematol* 2012;40:487–498.
 24. Sen GL, Webster DE, Barragan DI, et al. Control of differentiation in a self-renewing mammalian tissue by the histone demethylase JMJD3. *Genes Dev* 2008;22:1865–1870.
 25. Seenundun S, Rampalli S, Liu Q-C, et al. UTX mediates demethylation of H3K27me3 at muscle-specific genes during myogenesis. *EMBO J* 2010;29:1401–1411.
 26. Faralli H, Wang C, Nakka K, et al. UTX demethylase activity is required for satellite cell-mediated muscle regeneration. *J Clin Invest* 2016;126:1555–1565.
 27. Burgold T, Voituron N, Caganova M, et al. The H3K27 demethylase JMJD3 is required for maintenance of the embryonic respiratory neuronal network, neonatal breathing, and survival. *Cell Rep* 2012;2:1244–1258.
 28. Manna S, Kim JK, Baugé C, et al. Histone H3 lysine 27 demethylases Jmjd3 and Utx are required for T-cell differentiation. *Nat Commun* 2015;6:8152.
 29. Bosselut R. Pleiotropic functions of H3K27Me3 demethylases in immune cell differentiation. *Trends Immunol* 2016;37:102–113.
 30. Thompson CA, DeLaForest A, Battle MA. Patterning the gastrointestinal epithelium to confer regional-specific functions. *Dev Biol* 2018;435:97–108.
 31. Subramanian A, Tamayo P, Mootha VK, et al. Gene set enrichment analysis: a knowledge-based approach for interpreting genome-wide expression profiles. *Proc Natl Acad Sci U S A* 2005;102:15545–15550.
 32. Haber AL, Biton M, Rogel N, et al. A single-cell survey of the small intestinal epithelium. *Nature* 2017;551:333–339.
 33. Kim TH, Li F, Ferreira-Neira I, et al. Broadly permissive intestinal chromatin underlies lateral inhibition and cell plasticity. *Nature* 2014;506:511–515.
 34. Mead BE, Ordovas-Montanes J, Braun AP, et al. Harnessing single-cell genomics to improve the physiological fidelity of organoid-derived cell types. *BMC Biol* 2018;16:62.
 35. Muñoz J, Stange DE, Schepers AG, et al. The Lgr5 intestinal stem cell signature: robust expression of proposed quiescent ‘+4’ cell markers. *EMBO J* 2012;31:3079–3091.
 36. Robinson JT, Thorvaldsdóttir H, Winckler W, et al. Integrative Genomics Viewer. *Nat Biotechnol* 2011;29:24–26.
 37. Salic A, Mitchison TJ. A chemical method for fast and sensitive detection of DNA synthesis in vivo. *Proc Natl Acad Sci U S A* 2008;105:2415–2420.
 38. Kim CK, Yang VW, Bialkowska AB. The role of intestinal stem cells in epithelial regeneration following radiation-induced gut injury. *Curr Stem Cell Rep* 2017;3:320–332.
 39. Murata K, Jadhav U, Madha S, et al. Ascl2-dependent cell dedifferentiation drives regeneration of ablated intestinal stem cells. *Cell Stem Cell* 2020;26:377–390.e6.
 40. van Es JH, Sato T, van de Wetering M, et al. Dll1+ secretory progenitor cells revert to stem cells upon crypt damage. *Nat Cell Biol* 2012;14:1099–1104.
 41. Tetteh PW, Basak O, Farin HF, et al. Replacement of lost Lgr5-positive stem cells through plasticity of their enterocyte-lineage daughters. *Cell Stem Cell* 2016;18:203–213.
 42. Yu S, Tong K, Zhao Y, et al. Paneth cell multipotency induced by notch activation following injury. *Cell Stem Cell* 2018;23:46–59.e5.
 43. Buczaccki SJA, Zecchini HI, Nicholson AM, et al. Intestinal label-retaining cells are secretory precursors expressing Lgr5. *Nature* 2013;495:65–69.
 44. Jadhav U, Saxena M, O’Neill NK, et al. Dynamic reorganization of chromatin accessibility signatures during dedifferentiation of secretory precursors into Lgr5+ intestinal stem cells. *Cell Stem Cell* 2017;21:65–77.e5.
 45. Yan KS, Gevaert O, Zheng GXY, et al. Intestinal enteroendocrine lineage cells possess homeostatic and injury-inducible stem cell activity. *Cell Stem Cell* 2017;21:78–90.e6.
 46. Metcalfe C, Kljavin NM, Ybarra R, De Sauvage FJ. Lgr5+ stem cells are indispensable for radiation-induced intestinal regeneration. *Cell Stem Cell* 2014;14:149–159.
 47. Wilson CL, Ouellette AJ, Satchell DP, et al. Regulation of intestinal α -defensin activation by the metalloproteinase matrilysin in innate host defense. *Science* 1999;286:113–117.
 48. Liang S, Guo XK, Ou J, et al. Nutrient sensing by the intestinal epithelium orchestrates mucosal antimicrobial defense via translational control of Hes1. *Cell Host Microbe* 2019;25:706–718.e7.
 49. Ireland H, Houghton C, Howard L, Winton DJ. Cellular inheritance of a Cre-activated reporter gene to determine Paneth cell longevity in the murine small intestine. *Dev Dyn* 2005;233:1332–1336.
 50. Quelle DE, Cheng M, Ashmun RA, Sherr CJ. Cancer-associated mutations at the INK4a locus cancel cell cycle arrest by p16INK4a but not by the alternative reading frame protein p19ARF. *Proc Natl Acad Sci U S A* 1997;94:669–673.
 51. Jadhav U, Manieri E, Nalapareddy K, et al. Replicational dilution of H3K27me3 in mammalian cells and the role of poised promoters. *Mol Cell* 2020;78:141–151.e5.
 52. Hugues A, Jacobs CS, Roudier F. Mitotic inheritance of PRC2-mediated silencing: mechanistic insights and developmental perspectives. *Front Plant Sci* 2020;11:262.
 53. Reverón-Gómez N, González-Aguilera C, Stewart-Morgan KR, et al. Accurate recycling of parental histones reproduces the histone modification landscape during DNA replication. *Mol Cell* 2018;72:239–249.e5.

54. Hansen KH, Bracken AP, Pasini D, et al. A model for transmission of the H3K27me3 epigenetic mark. *Nat Cell Biol* 2008;10:1291–1300.
55. Coleman RT, Struhl G. Causal role for inheritance of H3K27me3 in maintaining the off state of a *Drosophila* HOX gene. *Science* 2017;356:1–11.
56. Laprell F, Finkl K, Müller J. Propagation of polycomb-repressed chromatin requires sequence-specific recruitment to DNA. *Science* 2017;356:85–88.
57. Marshman E, Booth C, Potten CS. The intestinal epithelial stem cell. *Bioessays* 2002;24:91–98.
58. Barker N, van de Wetering M, Clevers H. The intestinal stem cell. *Genes Dev* 2008;22:1856–1864.
59. Williams K, Christensen J, Rappsilber J, et al. The histone lysine demethylase JMJD3/KDM6B is recruited to p53 bound promoters and enhancer elements in a p53 dependent manner. *PLoS One* 2014;9:e96545.
60. Swigut T, Wysocka J. H3K27 demethylases, at long last. *Cell* 2007;131:29–32.
61. Gao N, White P, Kaestner KH. Establishment of intestinal identity and epithelial-mesenchymal signaling by Cdx2. *Dev Cell* 2009;16:588–599.
62. Saxena M, San Roman AK, O'Neill NK, et al. Transcription factor-dependent 'anti-repressive' mammalian enhancers exclude H3K27me3 from extended genomic domains. *Genes Dev* 2017;31:2391–2404.
63. Arcipowski KM, Martinez CA, Ntziachristos P. Histone demethylases in physiology and cancer: a tale of two enzymes, JMJD3 and UTX. *Curr Opin Genet Dev* 2016;36:59–67.
64. Kazakevych J, Sayols S, Messner B, et al. Dynamic changes in chromatin states during specification and differentiation of adult intestinal stem cells. *Nucleic Acids Res* 2017;45:5770–5784.
65. Salzman NH. Paneth cell defensins and the regulation of the microbiome: détente at mucosal surfaces. *Gut Microbes* 2010;1:401–406.
66. De Santa F, Narang V, Yap ZH, et al. Jmjd3 contributes to the control of gene expression in LPS-activated macrophages. *EMBO J* 2009;28:3341–3352.
67. Zhou VW, Goren A, Bernstein BE. Charting histone modifications and the functional organization of mammalian genomes. *Nat Rev Genet* 2011;12:7–18.
68. Bernstein BE, Kamal M, Lindblad-Toh K, et al. Genomic maps and comparative analysis of histone modifications in human and mouse. *Cell* 2005;120:169–181.
69. Lee S, Lee JW, Lee SK. UTX, a histone H3-lysine 27 demethylase, acts as a critical switch to activate the cardiac developmental program. *Dev Cell* 2012;22:25–37.
70. Miller SA, Mohn SE, Weinmann AS. Jmjd3 and UTX play a demethylase-independent role in chromatin remodeling to regulate t-box family member-dependent gene expression. *Mol Cell* 2010;40:594–605.
71. Nakato R, Sakata T. Methods for ChIP-seq analysis: a practical workflow and advanced applications. *Methods* 2021;187:44–53.
72. Wiedemuth R, Thieme S, Navratil K, et al. UTX – moonlighting in the cytoplasm? *Int J Biochem Cell Biol* 2018;97:78–82.
73. Kamikawa YF, Donohoe ME. The localization of histone H3K27me3 demethylase Jmjd3 is dynamically regulated. *Epigenetics* 2014;9:834–841.
74. Love MI, Huber W, Anders S. Moderated estimation of fold change and dispersion for RNA-seq data with DESeq2. *Genome Biology* 2014;15:550. <https://doi.org/10.1186/s13059-014-0550-8>.
75. Hulsen T, Vlieg J de, Alkema W. BioVenn – a web application for the comparison and visualization of biological lists using area-proportional Venn diagrams. *BMC Genomics* 2008;9:1–6.
76. Sadeh R, Launer-Wachs R, Wandel H, et al. Elucidating combinatorial chromatin states at single-nucleosome resolution. *Mol Cell* 2016;63:1080–1088.
77. Zang C, Schones DE, Zeng C, et al. A clustering approach for identification of enriched domains from histone modification ChIP-Seq data. *Bioinformatics* 2009;25:1952–1958.
78. Lun ATL, Smyth GK. csaw: a Bioconductor package for differential binding analysis of ChIP-seq data using sliding windows. *Nucleic Acids Res* 2016;44:e45.
79. Lun ATL, Smyth GK. De novo detection of differentially bound regions for ChIP-seq data using peaks and windows: controlling error rates correctly. *Nucleic Acids Res* 2014;42:e95.
80. Simes RJ. An improved Bonferroni procedure for multiple tests of significance. *Biometrika* 1986;73:751–754.
81. Stine RR, Sakers AP, TeSlaa T, et al. PRDM16 maintains homeostasis of the intestinal epithelium by controlling region-specific metabolism. *Cell Stem Cell* 2019;25:830–845.e8.

Received March 31, 2022. Accepted December 1, 2022.

Correspondence

Address correspondence to: Klaus H. Kaestner, PhD, MS, Department of Genetics and Institute of Diabetes, Obesity, and Metabolism, Perelman School of Medicine, University of Pennsylvania, Smilow Center for Translational Research, Room 12-126, 3400 Civic Center Boulevard, Philadelphia, Pennsylvania 19104-6145. e-mail: kaestner@penmedicine.upenn.edu.

Acknowledgments

The authors would like to thank the members of the Kaestner laboratory for their helpful discussions throughout this project, and specifically thank Ashleigh Morgan and Mark Tigue for their help with animal husbandry. The authors thank Drs Yitzhak Reizel, Mark Ferreira, and Catherine May for initial breeding of the mouse colony, and Dr Suzanne Shapira for her editing assistance. The authors also thank the Cell and Developmental Biology Microscopy Core for use of their microscopy services, as well as the Center for Molecular Studies in Digestive and Liver Diseases (P30 DK050306) for use of the Molecular Pathology and Imaging Core. The authors thank Penn's Next Generation Sequencing Core for their help with genomic sequencing and data analysis, and Dr Daniel Beiting and the DIY Transcriptomics course for help with data visualization. Finally, the authors thank Dr Biao Zuo and Inna Martynyuk of the Electron Microscopy Resource Laboratory for their help with transmission electron microscopy, Dr Khayrullo Shoniyozov of the Penn Small Animal Radiation Research Platform for his help with mouse irradiation studies, and Dr Elliot Friedman and Dillon Murphy of the Penn Microbial Culture and Metabolomics Core for their help and advice regarding experimental design.

CRedit Authorship Contributions

Hannah Kolev (Investigation: Lead; Methodology: Lead; Writing – original draft: Lead)

Avital Swisa (Methodology: Equal)

Elisabetta Manduchi (Formal analysis: Equal)

Yemin Lan (Formal analysis: Equal)

Rachel R. Stine (Investigation: Supporting; Methodology: Supporting)

Giuseppe Testa (Resources: Equal)

Klaus H. Kaestner, PhD, MS (Conceptualization: Lead; Funding acquisition: Lead; Writing – original draft: Supporting; Writing – review & editing: Lead)

Conflicts of interest

The authors disclose no conflicts.

Funding

This work was supported by National Institutes of Health grants R37DK053839 (K.H.K.) and F31DK126404 (H.M.K.), as well as the Penn Center for Molecular Studies in Digestive and Liver Diseases through the use of the Molecular Pathology and Imaging Core (National Institutes of Health grant P30DK050306) and the Penn Diabetes Research Center for the use of the Functional Genomics Core (National Institutes of Health grant P30-DK19525).